Artery/Vein Classification of Retinal Vasculature

By

Muhammad Usman
NUST201362753MSEECS61313F

Supervisor

Dr. Muhammad Moazam Fraz
NUST-SEECS(DoC)

A thesis submitted in partial fulfillment of the requirements for the degree of
Masters of Science in Computer Science (MSCS)

In

School of Electrical Engineering and Computer Science
National University of Science and Technology
Islamabad, Pakistan.
June 2016

Thesis Approval

It is certified that the contents and form of the thesis entitled **"Artery/Vein Classification of Retinal Vasculature"** submitted by **Muhammad Usman** student of **MSCS-3** have been found satisfactory for the requirement of the degree.

Advisor: **Dr. Muhammad Moazam Fraz (SEECS-DoC)**

Signature: _____

Date: _____

Committee Member 1: **Dr. Omar Arif (SEECS-DoC)**

Signature: _____

Date: _____

Committee Member 2: **Dr. Asad Anwar Butt(SEECS-DoC)**

Signature: _____

Date: _____

Committee Member 3: **Dr. Muhammad Munibullah(SEECS-DoC)**

Signature: _____

Date: _____

Dedication

To my mother and my big brother Dr. Sharif Khan.

CERTIFICATE OF ORIGINALITY

I hereby declare that the thesis titled "***Artery/Vein Classification of Retinal Vasculature***" my own work and to the best of my knowledge. It contains no materials previously published or written by another person, nor material which to a substantial extent has been accepted for the award of any degree or diploma at SEECS or any other education institute, except where due acknowledgment, is made in the thesis. Any contribution made to the research by others, with whom I have worked at SEECS or elsewhere, is explicitly acknowledged in the thesis.

I also declare that the intellectual content of this thesis is the product of my own work, except to the extent that assistance from others in the project's design and conception or in style, presentation and linguistic is acknowledged. I also verified the originality of contents through plagiarism software.

Author Name: Muhammad Usman

Signature: _____

Date: _____

Acknowledgments

Contents

Abbreviations and Symbols

A/V	Artery/Vein
ACC	Accuracy
AUC	Area Under Curve
AVR	Arteriolar-to-Venular Ratio
B-COSFIRE	Bar-selective Combination of Shifted Filter Responses
BAGGING	Bootstrap Aggregating
CAD	Computer-Aided Diagnosis
CHASE_DB1	Child Heart and Health Study in England_DataBase
CME	Cystoid Macular Edema
DoG	Difference-of-Gaussians
DR	Diabetic Retinopathy
DSM	Dome-Shaped Macula
FD-OCT	Fourier Domain-Optical Coherence Tomography
FOV	Field of View
FFA	Fundus Fluorescein Angiography
IRMA	Intraretinal Microvascular Abnormalities
KNN	K-Nearest Neighbours
MCC	Matthews Correlation Coefficient
ME	Macular Edema
NVD	Neovascularization of Disc
NVE	Neovascularization Elsewhere
OCT	Optical Coherence Tomography
OD	Optic Disc
ONH	Optic Nerve Head
PDR	Proliferative Diabetic Retinopathy
PM	Pathological Myopia
ROI	Region of Interest
ROC	Receiver Operating Characteristic
SD-OCT	Spectral Domain- Optical Coherence Tomography
SNR	Signal to Noise Ratio
SS-OCT	Swift Source- Optical Coherence Tomography
TD-OCT	Time Domain- Optical Coherence Tomography

List of Publications from MS Thesis

Published Journal Article

Usman, M., Fraz, M. M., & Barman, S. A. (2016). Computer Vision Techniques Applied for Diagnostic Analysis of Retinal OCT Images: A Review. *Archives of Computational Methods in Engineering*, 1-17. **Publisher: Springer Link, Impact Factor: 3.68**

Under-Review Article

Muhammad Usman, Muhammad Moazam Fraz "Artery/Vein Classification in Retinal Vasculature using Ensemble Classification".

Submitted to: *Computational and Mathematical Methods in Medicine*

List of Figures

List of Tables

Abstract

Blood vessels in the human retina are the only non-invasive window of human blood circulatory system. In recent years, researchers have found that changes in arteries and/or veins in the retinal vasculature are associated with various systemic diseases, such as hypertension, diabetes, cardiovascular or cerebral disorders. Classification of retinal blood vessels into arteries and veins is the prerequisite for the assessment of vascular changes for automatic detection of particular systemic disease. An ensemble classification based approach has been employed in this study to accurately discriminate between arteries and veins in retinal vasculature. The methodology is evaluated on a publically available dataset CHASE_DB1. It consists of 387 retinal vessels (193 arterioles, 194 veins) from 28 retinal images of multi-ethnic school going children in England. A comparative analysis of different classifiers is performed and showed that ensemble based classifier offers preeminent accuracy and used for analysis in this study.

Chapter 1

Introduction

Automatic detection of retinal impairments in retinal fundus images using digital image analysis techniques have great potentials and advantages, which leads to investigate a large number of images in small-time, minimize cost and bias than current observer-based approaches. Furthermore, it offers an automatic screening of different pathological conditions, such as diabetic retinopathy, in order to minimize the workload essential of skilled manual graders [1]. Several diseases, such as hypertension [2], diabetes [3] and cardiovascular pathologies [4] affect blood circulation and retinal vessels, thereby leading to either dilation or narrowing of main retinal arteries, veins and microvascular.

In addition, asymmetric changes in the diameter of the retinal arterioles and venules, as quantified by the arteriolar-to-venular ratio (AVR) [5], have significantly associated with several diseases such as stroke, coronary heart disease [6] and atherosclerosis [7]. Additionally, a low AVR has been correlated and a direct biomarker for diabetic retinopathy which is a leading cause of retinal impairment in developed countries [8], "This low AVR is caused by abnormal widening of the veins due to retinal hypoxia". Moreover, a high AVR has been linked with amyloid A levels, interleukin 6, high-sensitivity C-reactive protein [9] and with high cholesterol levels in the body [7]. Diseases of the pancreas can also cause unusual AVR [8].

Moreover to measures like AVR and the thicknesses of arteries and veins, other clinically important features are vascular tortuosity[10], junctional exponents [11], length-to-diameter ratios [1] and vascular bifurcation angles [12]. To facilitate these measurements and collect data on a large-scale number of images, we need to distinguish arteries and veins of retinal vasculature.

In general, arteries are bright red, have thicker walls, which reflect the light as a shiny central reflex strip [13]. Veins are darker and also have larger calibers than arteries. Vessel calibers can be disturbed by systemic diseases, therefore, could not be used as a reliable feature for artery/vein (A/V) classification [13]. Some other properties of the retinal vascular tree are that in the region near to optic disc (OD) arteries rarely cross arteries and the same for veins, but both categories can bifurcate to narrower vessels and can cross each other [13]. These features are shown in Fig. 1
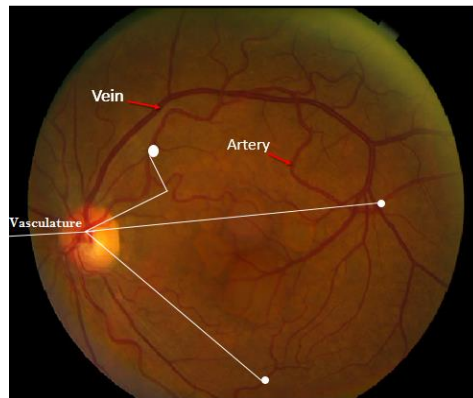
Fig. 1 Illustration of Arteries and Veins in fundus image: arteries are red bright carries oxygenated blood to retina while veins are darker and a bit wider than arteries, carries deoxygenated blood from the retina. Complete vessel tree of the retina is called vasculature[14].

Several imaging modalities such as optical coherence tomography, fluorescein angiography, and fundus photography can be used to capture retina of an eye. In this study,

fundus images are preferred for retinal vessel analysis, due to its several benefits such as lower cost, ease of use, and it conveniently allows telemedicine and remote diagnostics.

Our methodology is based on supervised learning. A pixel-based classification strategy is adopted. Decision trees based ensemble classifier is used for A/V classification. First of all, we segment blood vessels using B-COSFIRE filter [15] and extract centerline pixels using fast marching method [16]. Junction points are then identified and removed in both images to make vessel and centerline segments. Expert labeled ground truth has been used to extract a set of 34 local features for each centerline pixel. Finally, complete vessel segments are classified using the information of classified centerline pixels. The methodology is evaluated on CHASE_DB1 dataset [17]. According to the best of our knowledge, decision trees based ensemble classifier with CHASE_DB1 has been used for the first time for A/V classification. This technique is implemented in Matlab and run on the parallel computing-based system.

1.1 Aims and objectives of the project

The accurate measurement of retinal vessel parameters is an important problem in eye research, especially in retinal image analysis. Diseases can alter the width of portions, or the entire length, of retinal vessels, increase their curvature or tortuosity, and/or change their reflectance of light. To measure clinically important features and ratios, the first step is to precisely distinguish between arteries and veins. Aim or objective of the project is accurately classification or discrimination between arteries and veins in the retinal vasculature.

1.2 Organization of the thesis

Organization of the thesis is carried out as follows: In chapter 2, we presented related work on artery/vein classification and explored OCT modalities, it's working principles and terminologies because we have to take into account the quality of an image to investigate an ocular disease. In chapter 3, we explained our proposed methodology for A/V classification in detail. In chapter 4, Experimental results and performance analysis are presented. Discussions over future directions and conclusions are presented in chapter 5.

Chapter 2

Retinal Imaging Modalities and Diagnostic Retinal Image Analysis

In this chapter, we have presented a literature review of the different A/V classification approaches and also explained OCT (Optical Coherence Tomography) imaging modality. Analysis of different retinal disorders such as glaucoma, pathological myopia and diabetic retinopathy is also described in this chapter. Chapter is organized as follow: section 2.1 present literature review regarding A/V classification, section 2.2 explains the OCT modality while section 2.3 describes the analysis of different retinal diseases using OCT images.

2.1 Related work of A/V classification

Various methods have explored visual and geometrical features of the retinal vessels to enable distinction between arteries and veins and used them for A/V classification [8, 17-22]. Therefore, tracking of A/V in the retinal vasculature is possible and has been employed in some studies [17], [19] to analyze the vascular tree and classify the vessels.

2.1.1 Tracking-Based Approaches

A partly automatic approach for examining retinal vasculature was proposed by Martinez-Perez et al. [17]. In this approach topological and geometrical features of single vessel segments and subtrees are computed. First, vessel segmentation result is skeletonized, and

important points are identified. For the labeling, the user should first select root segment of the vessel tree to be tracked, the algorithm then searches for its terminal points and in the end, decide if the segment is artery or vein. A similar methodology was proposed by Rothaus et al. [19], in which they start from manually labeled vessel segments and defined a rule-based algorithm to disseminate the vessel labels as either vein or artery right through the vessel tree. This approach also uses existing vessel segmentation results. Grisan et al. [20] proposed a tracking-based artery and vein classification approach that classifies the retinal vessels in a pre-defined concentric region around the optic disc. The algorithm is designed in such a way that first divide the entire zone into four quadrants, and works separately on each of them. Finally, the algorithm propagates the classification outside the region, using the vessel structure reconstructed by tracking. Vazquez et al. [21] developed a methodology which integrates a colour-based clustering algorithm with a vessel tracking strategy. The clustering algorithm first divides the entire image of the retina into four quadrants, the detected vessels in each quadrant are then separately classified, and at the end, it integrates the results. Subsequently, a tracking technique based on a minimal path method has used to link the vessel segments situated at different radii to support the classification.

2.1.2 Graph-Based Approaches

A group has proposed a graph-based approach to constructing A/V trees [23]. They have used morphological features and vessel likelihood maps based graph search method. First, vessels are divided into centerline segments, and then the vessels network is constructed by identifying every landmark. Finally, graph search technique was used to separate the constructed network into A/V trees. Other researchers have recently employed similar techniques as well: Dashtbozorg et al [24], fist skeletonized the retinal vessels and

separated them into centerline segments. Then, a graph is constructed where every node indicates a junction point and edge indicates segment, the retinal vessel trees were built by defining the node types and vessel types together. However, this method uses a graph with static structure and local information about nodes in advance. Finally, the linear discriminant analysis (LDA) classifier has been applied to classify the entire vascular tree by determining the type of each junction point. Moreover, a recently published graph-based semiautomatic procedure proposed by Estrada et al [25] to construct retinal arteries and veins trees. First, they semi-automatically construct a graph from funds photographs, indicating retinal vessels, then classify it into artery and vein trees through maximizing the likelihood of A/V trees.

2.1.3 Supervised Learning-Based Approaches

In a further study, Li et al. [22] proposed a "piecewise Gaussian model" to identify vessel types and to describe the spatial distribution of vessel profiles. The model has also considered the central reflex. The features computed from the parameters of the model, employed with a minimum distance classifier based on the Mahalanobis distance to discriminate between arteries and veins. Kondermann et al. [8] employed two feature extraction methodologies and two classification approaches such as neural networks (NN) and support vector machines (SVM) to classify arteries and veins of retinal vasculature. One of the feature computation techniques is profile-based while the other is based on the definition of a region of interest (ROI) around the centerline points. The influential features have been selected through multiclass principal component analysis (PCA). Niemeijer et al. [18] presented an automatic approach to classifying retinal vessels into arteries and veins. They have used image intensity and derivative features and a classifier for this purpose. A set of features is computed for each centerline pixels and assigned a soft label,

indicating the probability that it is a vein pixel. The median of the soft labels of a centerline segment is assigned to each centerline pixel. They have found that k-nearest neighbor (KNN) generally offered the best result. In [26], the classification technique was improved as a step in computing the AVR value.

2.2 OCT Modalities and Terminologies

2.2.1 OCT Terminologies

OCT works by measuring the delay of reflected radiation similar to ultrasound and radar images. Depending on the importance of longitudinal (depth) and a crosswise direction, some scanning modalities have been employed to represent the cross-sectional information. These scanning modalities are classified as A-scan, B-scan and C-scan[18]. The nomenclatures used in OCT are similar to ultrasound terms. In ultrasound Axial-scan (A-scan) basically records two important factors of an echo: its amplitude and pulse transit time. In OCT systems, an A-scan can be measured by scanning the reference throughout the entire depth as illustrated in Fig. 2(a) and Fig. 3; but, due to innovations in performance and techniques, the entire distribution of A-scans can be measured at once without any reference scan. Same, B-scans can be measured by gathering several A-scans of diverse adjacent crosswise locations, and a collection of parallel B-scans can be used to gather a 3D dataset[19] as illustrated in Fig. 2(b) and Fig. 3. A C-scan can be acquired by scanning the sample along with several successive x and y directions at a fixed depth as shown in Fig. 2(c)which can offer a cross-sectional image at different depths.
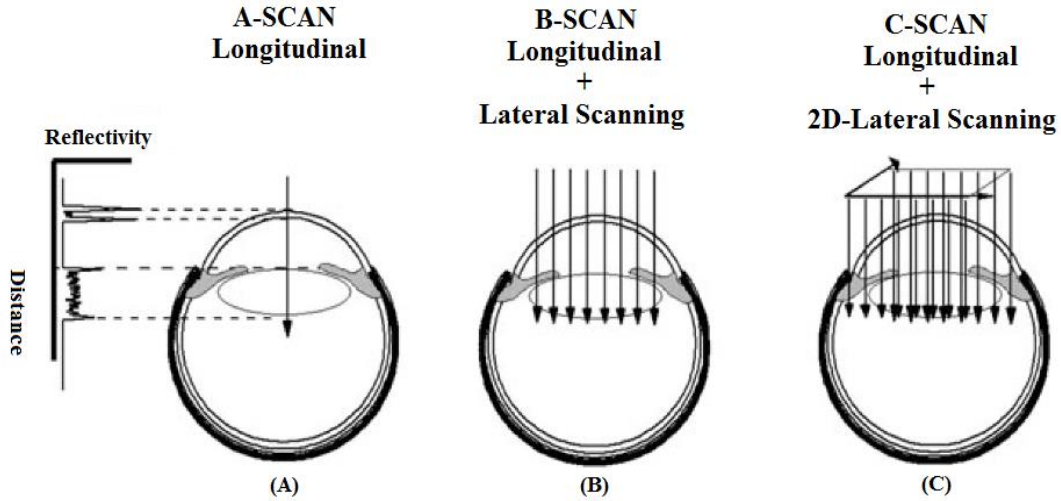
Fig. 2 Scanning terminologies. Diagrammatically representation of different scanning modalities in OCT[20]. An eye can be scanned just in a longitudinal manner in A-Scan (A) whereas in B-scan it is scanned in x-axis and y-axis direction at the same time (B). In C-Scan modality, an eye is scanned in three directions, such as in x-axis, y-axis and z-axis directions at the same time(C). Distance measures that how much deep the eye is penetrated while reflectivity measures the reflected illumination signals from the eye which could be used to construct an OCT image.
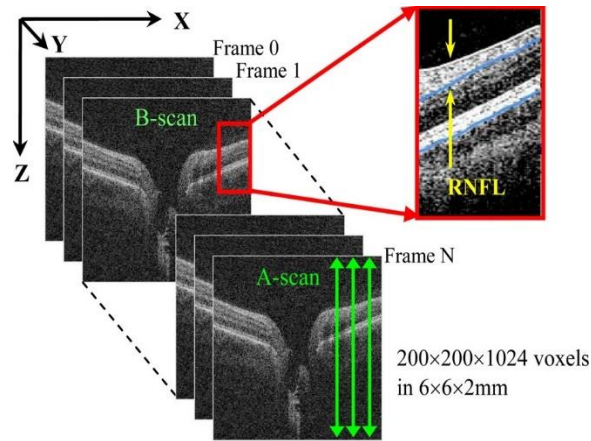
Fig. 3 OCT terminologies: Demonstration of A-scans, B-scans and a 3D OCT image of optic nerve head region. 3D OCT image composed of consecutive B-scans, each B-scan consists numerous A-scans [21]. The image in red rectangle illustrates retinal layers. Retinal Nerve Fiber Layer (RNFL, within yellow arrows) composed of retinal nerves which serve to transfer visual information from eye to brain.

2.2.2 OCT Modalities

In OCT the coherence-gated data related to the eliminatory volume of the scatters can be retrieved by either the Time Domain (TD-OCT) or Fourier domain (FD-OCT) principle[20, 22].

2.2.2.1 Time Domain OCT Systems (TD-OCT)

In these systems, the illumination source is divided initially at the beam-splitter into two components. One part is forwarded to the sample and the other is directed to a reference mirror. Finally, the back-reflected signals from both places are then re-channeled and join via the BS and are detected by a photodetector as illustrated in Fig. 4. OCT's first acquisition methodology was based on TD. Later improvements involved the FD principle for capturing OCTs. The key shortcoming of TD-OCT compared to FD-OCT is that the moving mirror at the reference arm causes slower capturing speed in TD-OCT[19]. Typical TD-OCT can capture 400 to 500 A-scans per second with an axial resolution of ~10 to 25 μm [23-26] and this low axial resolution leads to poor image quality as shown in Fig. 5. These systems are 40-110 times slower than commercially existing FD-OCT. FD-OCT can acquire 55,000 A-scans per second[27] whereas TD-OCT would need 1.3 seconds to capture 512 A-scans[23-26].
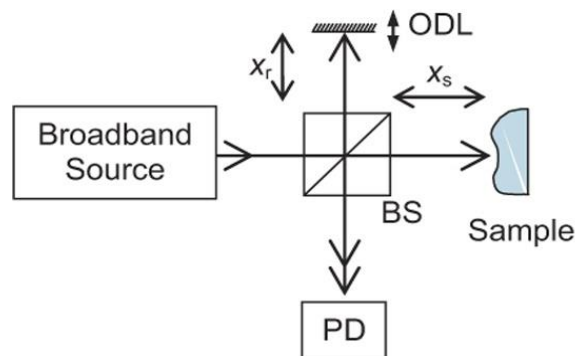
Fig. 4 Time Domain OCT principle. The light source has been divided into two parts such as Xr and Xs at

Beam-Splitter (BS) and forwarded them to sample and reference Optical Delay Line (ODL) surface.

Reflected signals from both points are then rechanneled at BS and detected by Photo Detector (PD)[28].
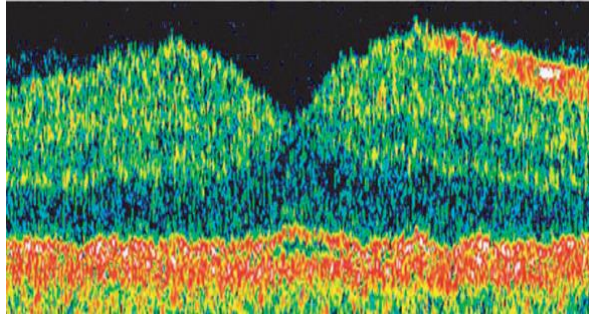
Fig. 5 Time Domain Stratus OCT image: ~10 mm axial resolution, 512 A-scans acquired in 1.3s, OCT

performed with a TD-based laboratory prototype[29].

2.2.2.2 Fourier Domain OCT systems (FD-OCT)

FD-OCT can be divided into two types namely: Spectral Domain OCT (SD-OCT) and

Swept-Source OCT (SS-OCT). Both SD-OCT and SS-OCT allow three-dimensional(3D)

imaging of tissues[30]. A brief overview of each of these FD-OCT types is given below.

2.2.2.2.1 Spectral Domain OCT (SD-OCT)

SD-OCT employs a broadband source and spectrometer based detection[30]. It is a major

work in the enhancement of OCT imaging speed and resolution, which led to an increase

in the number of A-scans/s possible. A value of 15,000 A-scans/s, was presented in

2003[31]. A system was presented with Fourier-domain detection, using a customized

spectrometer with a charge-coupled device (CCD) camera. And at that time, high-speed

line scan CCD cameras started to appear on the market, which used data transfer protocols

enabling work with a duty cycle of more than 90%. New systems using CCD cameras

(AViiVA-Atmel/E2V, Goodrich, Basler) made it possible to obtain scanning speeds of

18,000 A-scans/s in 2003[32], 30,000 A-scans/s in 2004 [33], and 50,000 A-scans/s in 2007

[34]. However, the real innovation in imaging speed with the use of SD-OCT was the application of a high-speed scan camera with a CMOS detector, revealed in 2008 by Potsaid et al. from MIT[35]. In experiments demonstrated at MIT, the highest speed of more than 300,000 A-scans/s has been shown with 1:5 mm axial range and 9 μm axial resolution. To give a fair comparison to other ophthalmic high-resolution SD-OCT systems keeping the range more than 1 mm and a resolution of approximately 2 μm, the CMOS-based SD-OCT system can run up to approximately 120,000 A-scans/s [35-37]. Fig. 6(a) shows a sample of SD-OCT image.

2.2.2.2.2 *Swept Source OCT (SS-OCT)*

SS-OCT uses a frequency swept laser and a high bandwidth balanced photo-detector to capture images [38]. This technique is also known as Optical Fourier Domain Imaging (OFDI) [39-41]. In 1997, an idea is presented in which a continuous wave chromium-doped laser has been used for fast tuning of wavelength on a wide bandwidth [42]. Later three main ideas were proposed to achieve high-speed tuning and these methods depend on the technique used for wavelength selection inside a short laser cavity of swept-source wavelength. First, is using a fast-rotating polygonal mirror founded by Yun et al. [43]. It was initially used for OCT imaging with a 15kHz sweep rate and later sweep rate emerging up to 115 kHz [44, 45] and is now available commercially (Santec) at a 50 kHz scanning rate with almost 100% duty cycle(A duty cycle is the percentage of one period in which a signal is active). The second concept is based on Diffraction-Grating-Coupled with a mechanically resonant galvo-scanner, this kind of laser was made by MIT and Thorlabs in a collaboration project in 2005 [40]. Currently, these light sources are available commercially from Thorlabs and provide up to 50,000 A-scans per second OCT imaging speed [46, 47]. The third concept of rapid tuning is based on fiber Fabry-Perot tunable

filters [48, 49]. To overcome shortcomings caused by buildup time of lasing in the cavity and achieve high tuning speed, the method of Fourier-domain mode locking (FDML) was presented by Huber et al. in 2005 [50]. As compared with conventional wavelength swept lasers, FDML lasers show improved noise performance, output power, coherence length, and higher maximum sweep repetition rate [50-52]. Fig. 6(b) illustrates a sample of an SS-OCT image.
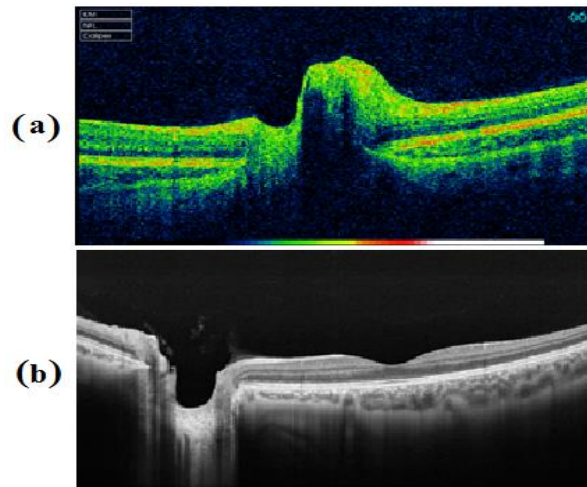
Fig. 6 SD-OCT and SS-OCT images: (a) SD-OCT images of optic nerve head captured by Topcon 3D OCT-1 Maestro machine [53]. (b) Swept Source OCT images of ONH by Topcon DRI OCT-1, Atlantis swept source OCT machine [54].

2.2.3 OCT Devices Manufacturer

FD-OCT images can be captured by a variety of devices. The most famous devices are manufactured by NIDEK CO, Optovue Inc., Carl Zeiss Meditec, Topcon, OPKO Inc. and Heidelberg Engineering [55-59]. Researchers and ophthalmologists need information regarding which OCT-instrument they should purchase for their requirements. The technical information of devices that is listed in Table 1 including the features of averaging and anterior segment potentials [60], would help individuals to invest in appropriate

Table 1 Technical details for commercially available OCT devices.

Name	Resolution (optical) axial transversal	A-Scans Scans /sec max. number for a B-Scan	Averaging Yes/No max number	Anterior segment	Follow-up	Normative database Nerve fiber layer Retina	Additional features
Nidek RS-3000	7 µm 20 µm	53.000 1024	Yes 50	With adaptor	Yes	Yes Yes	*SLO
Optovue OCT scanner	5 µm 15 µm	26.000 1024	Yes 50	With adaptor	Yes	Yes Yes	SLO, Color
Zeiss Cirrus 4000	5 µm 15 µm	27.000 4096	Yes 20	Without adaptor	Yes	Yes Yes	SLO
Topcon -2000	5-6 µm ≤20 µm	27.000 4096	Yes 50	With adaptor	Yes	Yes Yes	[1]IR-CCD, Color
Opko / OTI	6 µm 15 µm	27.000 1024	Yes 25	With adaptor	Yes	Yes Yes	SLO, Microperimetry
Heidelberg spectral	7 µm 14 µm	40.000 4096	Yes,100 Eye-tracker	With adaptor	Yes Eye-tracker	Yes Yes	SLO, Red-free, and [2]Flu. Ang.

*Confocal scanning ophthalmoscope, [1]InfraRed- Charge-coupled device, [2]Fluorescein Angiography

devices. However, technology is rapidly developing and therefore the information is subject to change.

The speed and amount of A-scans are essential, for both fast acquisition of 3D scans and acquisition of multiple A-scans/B-scans for averaging. A confocal scanning ophthalmoscope image (SLO image), an OCT image and fundus are common on most machines. A variety of different algorithms are used to align and register OCTs with fundus photographs for averaging purposes, these details are expressed by eye tracking in the table which representing a real time tracking. Normative databases and some additional characteristics may not be typical, but access is increasing for all machines.

2.3 Diagnostic analysis of retinal OCT images

2.3.1 Glaucoma diagnostic and examination from OCT

Glaucoma can be detected by three methods such as: (1) Abnormal Intra Ocular Pressure(IOP) measurement, (2) Abnormal Visual Field(VF) assessment, (3) Assessment of damaged ONH (measuring the CUP and Disk ratio) or Nerve Fiber Layer(NFL) [61]. Noncontact tonometry (air puff test) can be used to measure IOP but it is not a sensitive

and specific tool for glaucoma assessment because glaucoma can progress without IOP while the visual field has poor repeatability; according to John et al. [62] 85.9% of abnormal and reliable visual fields were not confirmed on retest.

Assessment of the ONH or NFL is more favorable than IOP and VF measurement. Igor et al. [63] showed that RNFL is the dominant parameter for glaucoma diagnosis and progress detection. Juan Xu et al. [64] have utilized 3D OCT volume to successfully classify early glaucomatous eyes. OCT volume is converted first to an adjusted 2D feature map by going through some steps. They have first segmented OCT layers and blood vessels from the 3D volume. In a second step, they have calculated a blood vessels map from segmented vessels, RNFL thickness map, RNFL reflectivity map and deviation map from segmented layers. In the third step, the vessel map is then minimized from the RNFL thickness map added to RNFL reflectivity map and the result is then combined with the deviation map to construct a 2D feature map (processed RNFL thickness map). After conversion of the 2D feature map into variable size superpixels as illustrated in Fig. 7, they have then employed a boosting algorithm for eye classification.
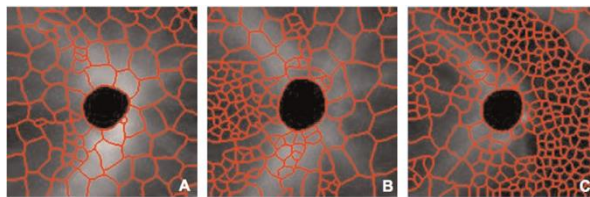
Fig. 7 Superpixel segmentation: (A) Result of a healthy eye, (B) glaucoma suspect, and (C) glaucomatous eye. Small superpixels show abnormal portion affected by glaucoma [64].

2.3.1.1 Disk-Cup segmentation

Normally there are two approaches which can be used to segment disk/cup from 3D ONH OCT images for glaucoma assessments. 1) The Pixel classification technique is applied to depth-columns of OCT voxels, manual planimetry is used to define reference standard from

stereo fundus images. 2) Segmentation of Neural Canal Opening (NCO) and cup using graph theoretical approach from 3D OCT images [65]. Fig. 8 illustrates the segmentation results of these techniques and have been reviewed one by one below.
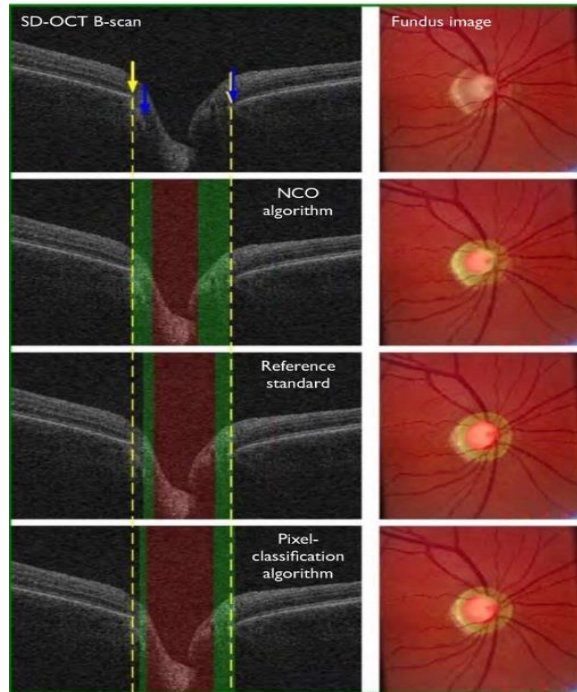
Fig. 8 Disk-Cup segmentation techniques and their results: Shown differences between structure-based segmentation of NCO/cup on OCT (second row), glaucoma expert definition of optic disc margin and cup from manual planimetry (third row) and segmentation optic disc/cup from OCT using pixel classification algorithm (bottom row). Yellow arrows indicate the position of NCO from the algorithm (with a dashed yellow line indicating projected NCO position). Blue arrows indicate clinical disc margin from Reference standard. Green and red colors indicate each method's projected rim and cup regions, respectively [65, 66].

For the pixel classification technique, a number of studies [67-69] have been performed. ONH centered scans of the SD-OCT images have been used by Lee et al. [68] to segment the optic disc cup and the neuroretinal rim. They developed a new method. In their proposed methodology they first segment three inner retinal layers with the help of a fast multiscale 3D graph searching method. Then, to remove some motion artifacts and to

have a consistent shape across layers of the retina of the OCT volume were flattened. Finally, a K-NN classifier is trained by the features derived from OCT voxels and intraretinal layers to categorize which A-scan in OCT volume belongs to the optic disc cup, background, and neuroretinal rim. In a further study, a fully automatic and fast technique proposed by L. Kyungmoo et al. [67] to segment the optic cup and rim from 3D SD-OCT volumes, they have been performed automatic planimetry directly from close to isotropic SD-OCT scans. In their proposed methodology, four intraretinal layers were segmented with the help of a fast multiscale 3D graph search method. Then, the segmented layers are flattened to get a consistent ONH shape. A total of fifteen features has been extracted from the segmented retinal layers and the voxel intensities for the training of the classifier. Lastly, they used a convex hull-based method to incorporate prior knowledge of the shapes of the cup and neuroretinal rim in the algorithm. Performance evaluation of the algorithm is presented by Fig. 9. In general, the methodology described in [67] accomplished results not essentially unique from expert analysis of the cup and rim boundaries of the ONH. Total 27(14 right eye scans and 13 left eye scans from 14 patients) retinal OCT volumes of optic nerve head centered have been used for the experiment by employing leave-one-subject-out approach, the unsigned error has been encountered for ONH cup and rim were 2.52±0.87 pixels and 2.04±0.86 pixels, respectively.

For the graph theoretic approach of ONH segmentation, a list of studies [66, 70-72] has been proposed to segment NCO and cup directly from 3D OCT images. A new scheme is presented by Hu et al [70] based on graph theoretic approach in which they segment the ONH. A small slice surrounding the Brunch's Membrane Opening (BMO) plane is utilized to create 2D projection planer images. Since there are a large number of vessels in an eye

which makes it difficult to segment exact information, to suppress vasculature effects they used segmented vessels by adjusting the polar cost function and remedy the segmentation difficulty. In a further study, Hu et al. [71] explore correspondence and inconsistency between NCO-based matrix and clinical disc margin. They have developed an automatic system to segment cup and NCO at the stage of Bruch's Membrane (BM) complex in SD-OCT volumes. In further improvements, Hu et al. [66] directly segment the NCO in SD-OCT volumes. In their methodology, they first creating a projection image at the level of the BM/RPE plane and then simultaneously detecting the NCO and cup margins at the level of this plane using a graph-theoretic approach. Using the disc margin as defined by three glaucoma specialist on fundus images as the reference standard, they have found mean unsigned and signed border error 0.084±0.044 mm and 0.030±0.061 mm, respectively. "The correlations of the linear cup-to-disc (NCO) area ratio, disc (NCO) area, rim area, and cup area of the algorithm with the RS were 0.85, 0.77, 0.69, and 0.83, respectively. It was not expected that the projection NCO position would perfectly correspond to the optic disc margin as defined on manual planimetry".as presented in Fig. 8.

(a)   (b)   (c)   (d)
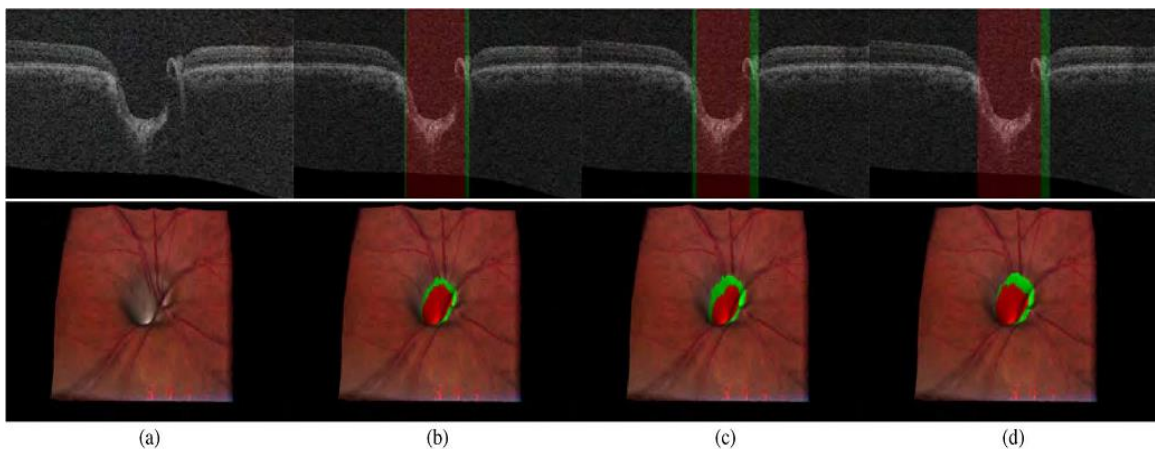
Fig. 9 ONH segmentation performance: unsigned error for OD cup is (0.038 mm) and for the neuroretinal rim (0.026 mm)]. From top to bottom, X-Z scans of OCT volume and 3-D rendering of a stereo color photograph. (a) Without any overlap. (b) Overlapped with the result from contextual K-NN classifier with convex hull-based fitting. Optic disc cup is in the red and neuroretinal rim is in green. (c) Overlapped with a reference standard. (d) Overlapped with manual segmentation from the second observer.

2.3.2 Analysis of pathological myopia from OCTs

In order to analyze pathological myopia with the help of OCT imaging modality. It has been found [73] that visual field flaws were greatly observed in eyes with type IX staphyloma which is the type with a ridge-like protrusion temporal to the optic disc. It has been discussed as well in PM manifestations that the shape of the sclera is significantly interrelated with myopic lesions. This information suggests that eye shapes and malformations, are most probably associated with the growth of the myopic lesions and examination of sclera will lead to an analysis of pathological myopia.

To the best of our knowledge two papers Imamura et al. [74] and Maruko et al. [75] have reported on the advent of the sclera in the macular area by OCT, these works have basically highlighted that in-vivo examination of the sclera of an example can be explored by OCT images. Imamura et al. [74] have employed Enhanced-Depth Imaging OCT (EDI-OCT) for their experiments and concluded that subfoveal sclera was thicker with a Dome-Shaped Macula (DSM) in highly myopic eyes. Maruko et al. [75] have computed scleral thickness at the posterior segment, they have determined that subfoveal sclera was thicker than superior and inferior part of the sclera. A total of nine SS-OCT images of Tilted-Disc Syndrome (TDS) of different subjects with average axial length 24.89 ± 1.05 mm has been used for their experiments. Ohno-Matsui et al. [76] have analyzed morphological characteristics and scleral contour of the sclera using SS-OCT images of highly myopic

subjects. It has been shown that in 57% of myopic subjects, the entire layer of the sclera was clearly visible and also revealed that the contour of the sclera could be divided into four distinct inner scleral patterns such as central fovea is on slope and disposed toward the optic nerve, symmetrical and asymmetrical curvature around the fovea, and sclera is irregular and does not have a smooth curvature. These patterns are illustrated with the help of Fig. 10. Analysis of these four curvature patterns showed that some of them were significantly related to myopic lesions. Results and discussion expressed that shape of highly myopic eyes is distorted which further leads to the growth of vision-threatening problems in patients having pathologic myopia. Fig. 11 shows the observation of sclera in high myopic eyes with the help of SS-OCT. Lim et al. [77] have demonstrated by a comparative study that SS-OCT is useful for imaging the posterior staphyloma of pathological myopia and providing greater details rather than SD-OCT.
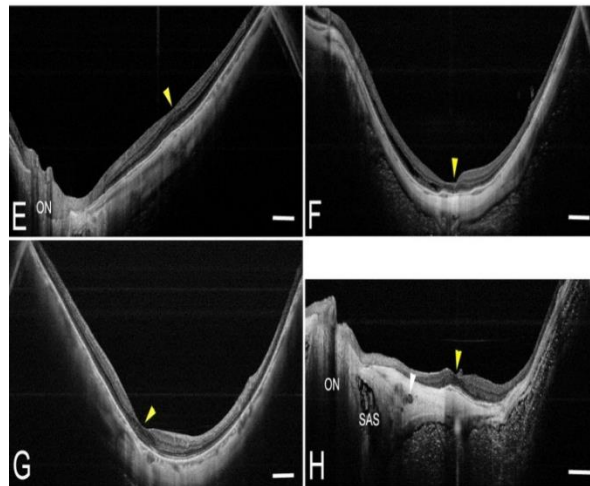
Fig. 10 Four different patterns of inner scleral curvature in highly myopic eyes: (E) The central fovea (arrowhead) is on the wall of the slope inclined toward the optic nerve. (F)The curve is symmetrical around the fovea (arrowhead), and the fovea is situated on the bottom of the posterior segment of the eye. (G)Asymmetrical curvature around the fovea, the fovea (arrowhead) is on the slope and the sclera is strongly bowed posteriorly. (H)The sclera is irregular and does not have a smooth curvature. The fovea is

shown by the yellow arrowhead. Intra scleral artery is shown by a white arrowhead. ON, optic nerve; SAS, subarachnoid space [76].
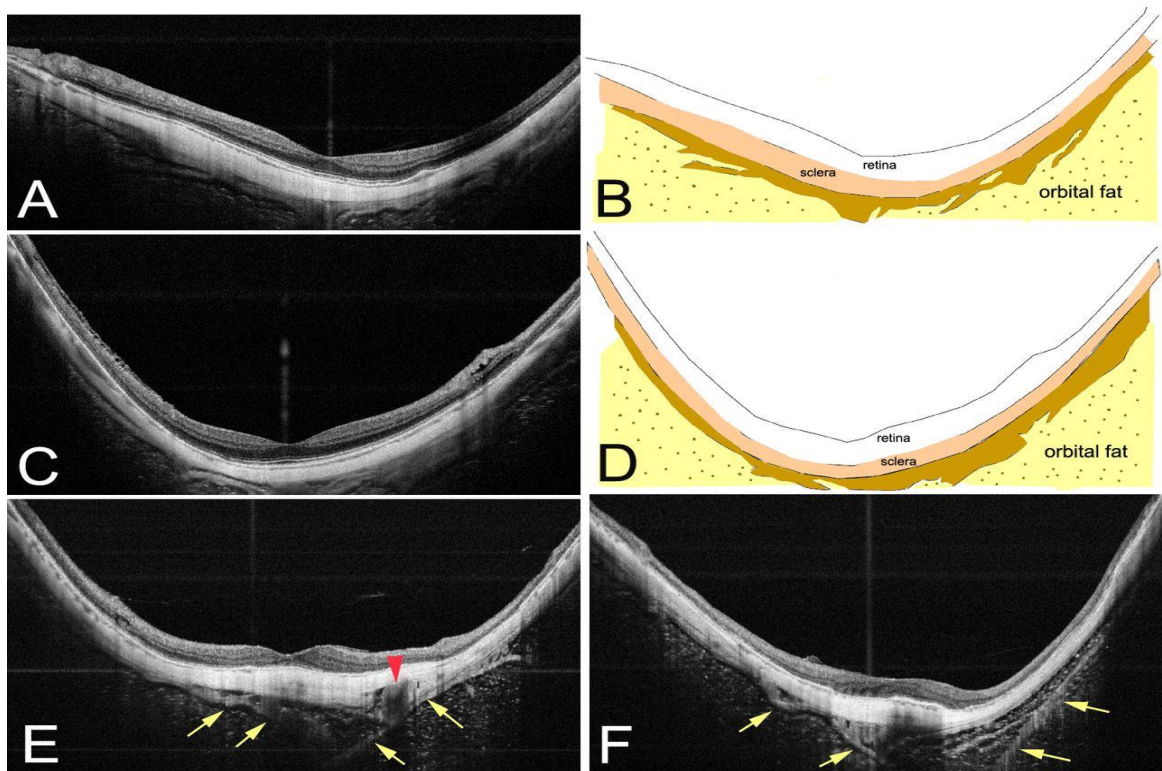
Fig. 11 Observations of the sclera and Tenon's capsule in highly myopic eyes by SS-OCT: (A, C) the sclera is observed as the highly reflective tissue outside the very thin choroid. A less reflective tissue can be seen outside the sclera. The orbital fat tissue is also observed as grayish tissue with many dots. (B, D) Schematic drawings of (A) and (C), respectively, with the tissues labeled. The sclera is colored orange and the tissue outside the sclera, suggestive of Tenon's capsule and episclera, is colored brown. (E, F) The fibers (arrows) of Tenon's capsule appear to spread and blend into the orbital fat tissue posteriorly. Cross sections of episcleral blood vessels can be seen posterior to the sclera (arrowhead, E) [76].

2.3.3 Diagnostic analysis of diabetic retinopathy from OCT images

Standard OCT has turned into an important modality in the assessment and observation of diabetic retinopathy [78]. It allows the clinician to detect and monitor neovascularization in various stages of Proliferative Diabetic Retinopathy (PDR) [79-82]. OCT scans are

highly useful in nursing for subtle cases diabetic macular edema, which is a principal cause of diabetic type blindness [83]. Fig. 12 illustrates the macular region OCT samples of normal and diabetic retinopathy affected eyes.
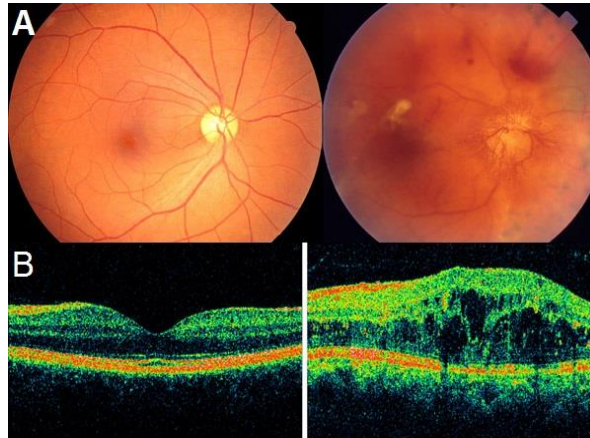
Fig. 12 Normal vs. Diabetic Retinopathy: (A) Traditional fundus photography images (B) OCT images, Retinal swelling (right) is a common cause of visual blurring in patients with diabetic retinopathy. The quantitative measurement of retinal thickness by OCT can improve management of therapies and decrease unnecessary or costly treatments [84].

OCT images could be used to detect cystoid fluids because they have the capability to analyze different layers of the retina. Cystoid Macular Edema (CME) is a painless ocular disorder caused by diabetes, its manifestation is when multiple cyst-like (cystoid) areas of fluid appear in the macula and cause retinal swelling or edema [85]. Wilkins et al. [86] proposed novel techniques to segment retinal-cysts without additional digging for DR detection, they have expressed that OCT images are Fourier domain in nature and could be greatly degraded by noise while capturing which leads to poor Signal to Noise Ratio (SNR) and would affect accuracy of segmentation [86].

The clinical utility of Doppler OCT to evaluate the 3-dimensional neovascular complexes in PDR is exploited by Miura et al. [87]. They have performed a comparative evaluation on why to practice Doppler OCT as an alternative to fluorescein angiography

for PDR assessment, stated that Doppler OCT is noninvasive, provides 3D information of neovascularization and impervious to leakage from new vessels, while fluorescein angiography is still important to assess diabetic retinopathy but it cannot provide 3D information and is impeded by fluorescein leakage from new vessels [87].
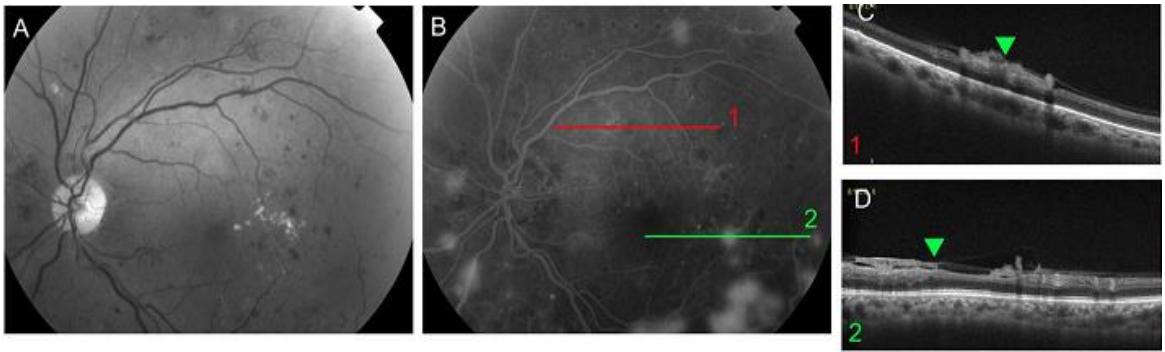
Fig. 13 IRMA and NVE lesions identification: (A) Red free photo of a left eye. (B)Fluorescein angiogram (late). There is leakage from the areas of neovascularization. The red line indicates the location of the corresponding OCT scan in (C); the horizontal green line indicates the location of the corresponding OCT scan in (D). IRMA lesion is shown in (C). NVE is shown in (D) [80].

Muqit et al. [79] have highlighted the importance of OCT for DR analysis from the most practical point of view. It has been observed that in current clinical practice, biomicroscopy and fundus photography are two basic methodologies to evaluate neovascularization; but these approaches have insufficient intelligence [88] to detect early stages of new vessels development. According to [79], OCT delivers significant information about the 3-dimensional structure of the neovascular complex in PDR and it has the strength to detect early stages of DR. A detailed comparative analysis of Neovascularization of Disc (NVD) from FD-OCT, fluorescein angiogram, and fundus images are demonstrated by Fig. 14. Cho et al. [80] inscribed in their study that with OCT, it is now achievable to estimate the disruption of the inner limiting membrane (ILM) and the breach of the posterior hyaloid

associated with Neovascularization Elsewhere (NVE) or NVD. Though, whether Intraretinal Microvascular Abnormalities (IRMA) and NVE can be distinguished on SD-OCT has not been established. Identifications of IRMA and NVE lesions in OCT are illustrated by Fig. 13.
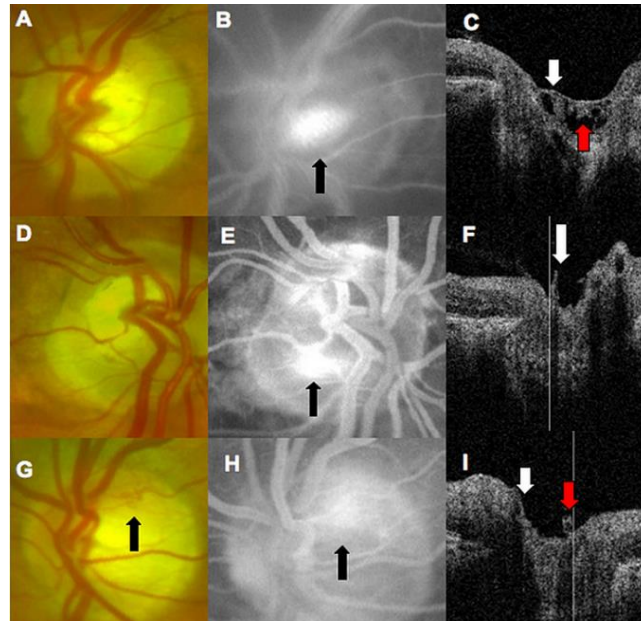
Fig. 14. NVD assessment: (A) fundus photograph of (NVD), with no visible signs of new vessels. (B) Fluorescein angiogram showing leakage from NVD (black arrow). (C) Fourier-domain optical coherence tomography (FD-OCT) shows Hyper-reflective branching NVD loops within the optic disc cup (red arrow), and the complex is attached to the outer aspect of the posterior hyaloid (white arrow). (D) The color photograph shows clinically visible, early new vessels on the disc. (E) Fluorescein angiogram confirms NVD leakage at the center of the optic disc cup (black arrow). (F) FD-OCT shows a hyper-reflective loop containing tiny hypo-reflective spaces that arise from the inner aspect of the neuroretinal rim. This represents the NVD complex (white line marker and arrow) shown on fundus fluorescein angiography (FFA). (G) Colour fundus photograph of early, mild Neovascularization at the disc (NVD, black arrows) and leakage on FFA (H). (I) The FD-OCT showed neovascular loops consisting of a hyper-reflective complex containing tiny hypo-reflective spaces (white line marker and red arrow). The NVD loops are attached to the outer aspect of the posterior hyaloid (white arrow) across the optic disc head and arise from the base of the optic disc cup. [79]

Chapter 3

The Methodology

This section describes our methodology for A/V classification. We presented a methodology as described in Fig. 15, for automatic classification of arteries and veins in retinal vasculature. we pass through some algorithmic steps: first of all, retinal vasculature was segmented using the B-COSFIRE algorithm, retinal skeletonization of the segmented vasculature was then computed using fast marching method to get vessels centerline pixels. Segmented vasculature and centerline pixels were divided at junction points to extract their segments. Finally, centerline pixels are classified using ensemble based classifier and more than 50% labeled pixels based criteria is used to label a specific vessels segment. A classified vasculature tree was built iteratively going through labeled vessel segments.
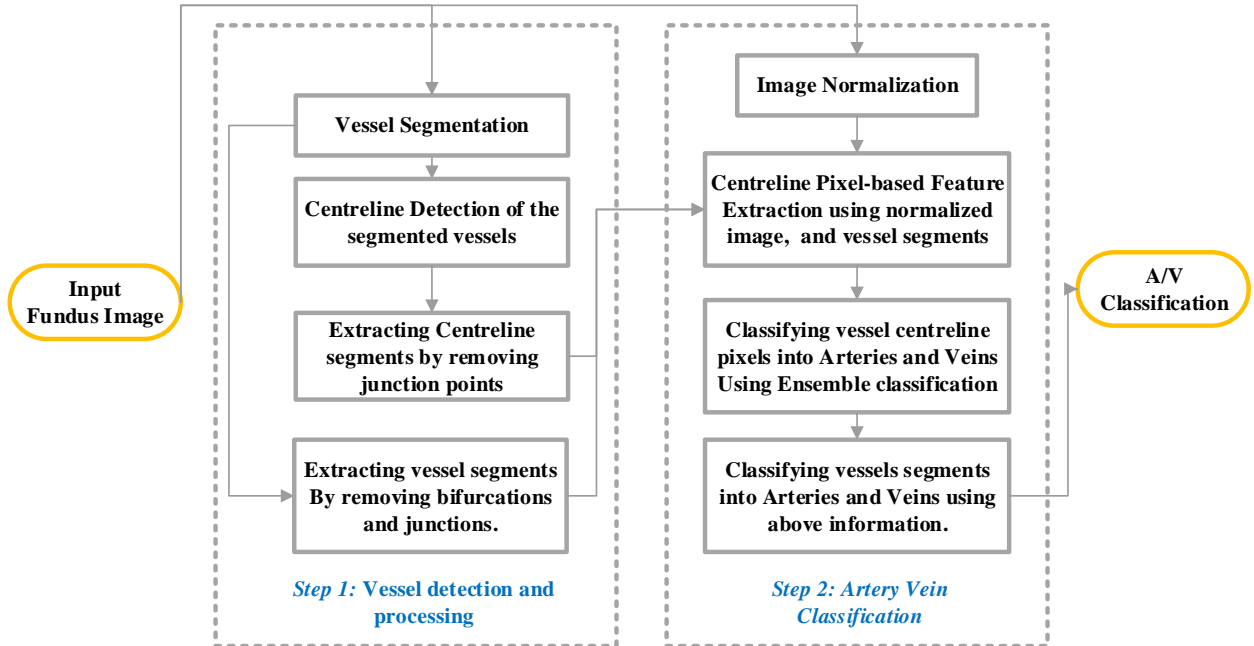
Fig. 15. The methodology of the proposed algorithm

3.1 Retinal Blood Vessel Segmentation

Automatic segmentation of retinal blood vessels from retinal fundus images is an essential processing step to detect retinal vascular changes. A measure of vessel-ness for each pixel in the retinal image is computed by bar-selective COSFIRE filter or B-COSFIRE for short [15]. B-COSFIRE uses a computational model, known as Combination of Receptive Fields (CORF) of a simple cell in visual cortex [89], and implementation of such model is called Combination of Shifted Filter Responses (COSFIRE) [90]. It is a non-linear trainable filter in nature, lenient to small deformations and to rotation variations. It achieves orientation selectivity by multiplying the output of a group of Difference-of-Gaussians (DoG) filters, whose supports are aligned in a collinear fashion. These DoG filters return high responses to intensity changes in the input image. Fig. 16(c) illustrates the principle design of the proposed B-COSFIRE filter that is configured to be selective for a vertical bar. Fig. 16(b) illustrates the responses of the B-COSFIRE filter to an image of CHASE_DB1 dataset [17].
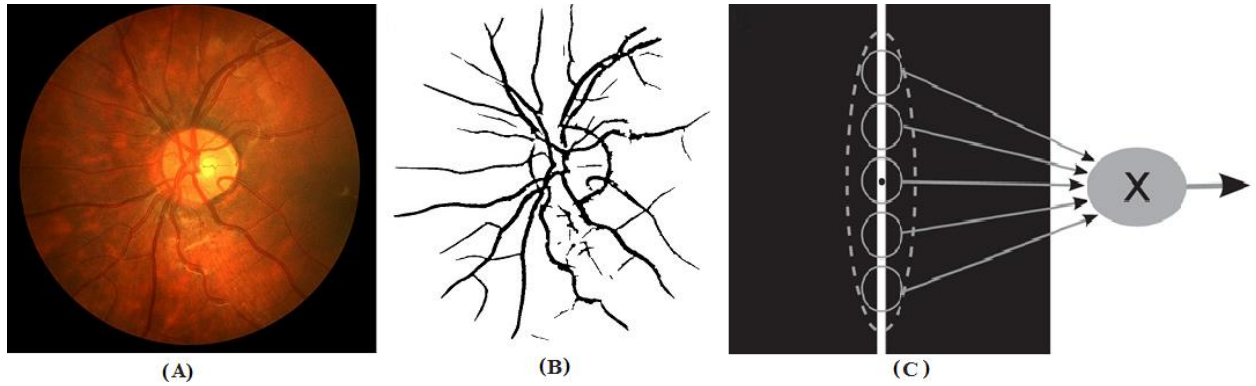
Fig. 16 Demonstration of B-COSFIRE filter: (A) is an original image [Image_01L of CHASE_DB1] and (B) is the vessel segmentation result through B-COSFIRE filter. (C) Sketch of the B-COSFIRE filter. The black spot in the middle of the white bar indicates the center of the filter support which is illustrated as a dashed ellipse. B-COSFIRE filter combines the responses from a group of DoG filters (represented by the solid circles) by multiplication.

3.2 Retinal Vessel Skeletonization

Representing a two or 3-dinensional data through constructing a centerline spinning tree is called skeletonization [91]. It allows easier manipulation and mining of information about the objects. A precise skeleton of an object could be used for object representation and registration. For example, an accurate computation of width, volume and length of the human organs, such as spinal cord and measurements of retinal vessels in funds and 3D-OCT images [92, 93], is possible by determining the skeleton of the organ. Furthermore, Junction points in retinal vessel skeleton can be used as a stable landmark for registration of fundus photographs [94].

To calculate retinal vasculature skeleton we employed a bit improved version of Robert Van Uitert et al. [16] algorithm. They have developed an efficient algorithm for 3D medical volumes skeletonization by employing fast marching method presented by Sethian [95], with time complexity O(kn log n). Where k represents the number of branches in the skeleton and n is the number of voxels in the data set. We used their algorithm for 2D

retinal vasculature skeletonization with fast marching method proposed by M. Sabry Hassouna et al. [96]. And, the extracted continuous vessel skeleton is then digitized by rounding the skeleton points to get single pixel wide centerline.

"Distance from each point inside an object to the closest boundary point is called distance filed". This proposed algorithm required a distance field of the object, such as the combine results of [96] and [97], to construct a skeleton the object. Remaining part of the algorithm has been explained in comprehensive by [16]. The outcome of the algorithm is presented in Fig. 17.
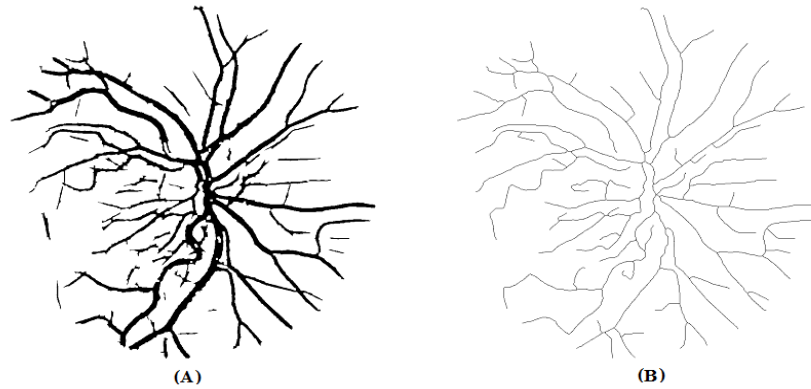
Fig. 17 Demonstration of vessel skeletonization using Fast Marching method.

3.3 Vessels and Centerlines Segments Extraction

The detection of junction points in the vessel tree of a retinal fundus image, commonly referred as vascular bifurcations and crossovers, is one of the basic steps in this analysis. Our strategy is based on to divide retinal vessels and their centerlines into segments at junction points. Afterward, to compute computer understandable ground truth, each segment is labeled as Artery/Vein from AV marked images of the CHASE_DB1. The vascular trees were built by iterating through the vessel segments.

3.3.1 Vessels Segments Extraction

Many researchers have recommended that retinal branching pattern, especially arterial branching pattern is governed by principles of optimality such as minimization of the pumping power, lumen surface, endothelial drag, and lumen volume [98, 99]. Vessel bifurcation angles and diameters are basic and important bifurcation features [100]; Fig. 18 explains the scenario. The branching angles and relative diameters are proposed to be designed to optimize the efficiency of the entire vascular network. Vessel junction points in this study have been computed by the same procedure theoretically described by Al-Diri et. al [100]. To get vessel segments, the detected junction points are dilated on an empty image, AND operation is then performed between inverted dilated points and the original image. Fig. 19(A) presents the result.
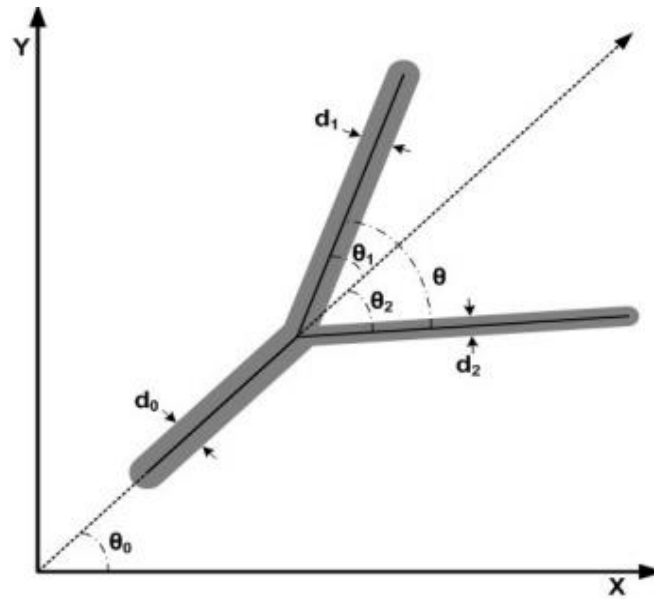
Fig. 18 Vessel bifurcation features: (di) is the diameter and (θ, θi) are branching angles.

According to some of these principles that k power law could be used to predict branching geometry:

$$r_0^k = r_1^k + r_2^k ,\qquad(1)$$

Where k is the junction exponent, r is the radius of the vessel, and d=2r is the vessel diameter. For asymmetry branching ratio [101], the power law can be expressed as:

$$\alpha = \frac{d_2^2}{d_1^2},$$

(2)

These features include the area ratio:

$$\beta = \frac{\left(d_1^2 + d_2^2\right)}{d_0^2} = (1+\alpha)(1+\alpha^{k/2})^{-2/k}$$

(3)

The bifurcation index:

$$\lambda = \frac{d_2}{d_1}$$

(4)

The diameter ratios:

$$\lambda_1 = \frac{d_1}{d_0} = (1+\alpha^{k/2})^{-1/k} \text{ and } \lambda_2 = \frac{d_2}{d_0} = \alpha^{1/2}(1+\alpha^{k/2})^{-1/k}$$

(5)

The bifurcation angels for minimum pumping power and lumen volume:

$$\cos\theta_1 = \frac{\lambda_1^{-4} + 1 - \lambda^4}{2\lambda_1^{-2}} ; \cos\theta_2 = \frac{\lambda_1^{-4} + \lambda^4 - 1}{2\lambda^2\lambda_1^{-2}}$$

(6)

And for minimum drag and lumen surface:

$$\cos\theta_1 = \frac{\lambda_1^{-2} + 1 - \lambda^2}{2\lambda_1^{-1}} ; \cos\theta_2 = \frac{\lambda_1^{-2} + \lambda^2 - 1}{2\lambda\lambda_1^{-1}}$$

(7)

3.3.2 Centerline Segments Extraction

The centerline of segmented vasculature which was computed in section 3.2, is divided into centerline segments at junction points. These junction points such as crossing and bifurcation points are detected by counting the neighborhood of each pixel. The entire centerline image has been scanned to analyze the neighbors of each pixel p (x, y) for eight-connectivity. The Intersection number ln(x,y) for each pixel p(x,y) is computed by eq (8)

[102], so that pixel p(x,y) can be marked as crossover if ln(x,y) =4, bifurcation if ln(x,y)=3, vessel internal point if In(x,y)=2, and vessel end point if ln(x,y)=1

$$\ln(x, y) = 0.5 * \left[\sum_{i}^{8} \left| N_i(x, y) - N_{i+1}(x, y) \right| \right]$$ (8)

Where N_i (x, y) are the neighbors of the analyzed point, p (x, y). The result is demonstrated by Fig. 19(B)

(A)   (B)
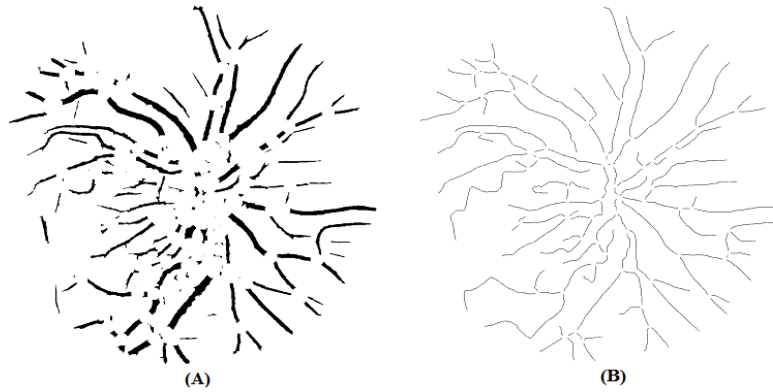
Fig. 19. The extraction of vessel and centerline segment by removing junction points.

3.4 Classification into Arteries and Veins

The extracted vessel segments need to be classified to either artery or vein class so that to enable analysis of the arteries and veins in the retinal digital fundus image. First of all, an expert indicated whether a given major vessel was an artery or vein for each of the training images. For classification, we have employed supervised classification, i.e., trained with examples and used vessel intensity features in order to allow the final discrimination between A/V classes. After a onetime training procedure, the training model is used to classify unseen centerline pixels into either arteries or veins. And labels of those pixels are then used for complete vessel segment classification.

3.4.1 Feature Vector

In general, we picked up color features to discriminate between arteries and veins. Arteries are red bright while veins are darker relatively. These features distinguish color and intensity variation in the vessel. The feature set has been normalized to zero mean and unit standard deviation to avoid bias by eq. (9) [103].

$$X' = \frac{X - \bar{X}}{\sigma} \qquad (9)$$

Where X' is the normalized feature vector, X is the extracted feature vector, $\bar{X}$ and σ are the mean and standard deviation of the feature vector, respectively.

Table 2 Feature set extracted for each centerline pixel.

Fea-Nr.	Features
1-3	Red, Green and Blue intensities under the centerline pixel
4-6	Hue, Saturation and Intensity under the centerline pixels.
7-9	Mean of Red, Green and Blue intensities across the vessel segment.
10-12	Mean of Hue, Saturation, and Intensity in the vessel segment.
13-15	Standard deviation of Red, Green and Blue intensities in the vessel segment.
16-18	Standard deviation Hue, Saturation, and Intensity in the vessel segment.
19-22	Maximum and minimum of Red and Green intensities in the vessel segment .
23-30	Intensity of the centerline pixel in a Gaussian blurred ($\sigma = 2, 4, 8, 16$) of Red and Green plane.
31-34	Intensity of the centerline pixel in a Steered second Gaussian derivative($\sigma = 2, 4, 8, 16$) of the fundus image.

3.4.2 Ensemble Classifier

Ensemble learning [104] is a procedure by which several classifiers are deliberately constructed and combined to solve a specific machine learning problem. The primary aim of ensemble-based classification is to minimize the likelihood of unfortunate selection and maximize the classification performance of a particular model. The ensemble approach combines the predictive performance of several weak models into a high-quality ensemble model or predictor. In this study, decision trees are used as classification models and predicted results of these weak models are combined using bagging algorithm.

3.4.2.1 Bagging Algorithm

Breiman's bagging, short for bootstrap aggregating, offers an amazingly good predictive performance and pretty simple to implement [105]. It is one of the most powerful classification idea presented in the past 20 years. Initially, it was proposed for classification and later extended to regression. The algorithm randomly draws multiple subsets from the whole training set using bootstrap, such that sampling with replacement. Each training subset is then used to train a different classifier or model. Decisions of these classifiers are then combined by taking majority voting to make a single decision.

3.4.3 Training Phase

Illumination on retinal images during capturing are often non-uniformly stretched, that exhibit contrast variability and local luminosity. To make the classification more accurate and robust, each image of the dataset has been normalized using the technique presented by M. Fracchia et al. [106]. This approach estimates the background contrast and luminosity deviations and uses them for normalization of the whole image.

After that, an ensemble based classifier has been trained using expert labeled vessels to distinguish between both classes of the centerline pixels. There are total 61972 observations in the training dataset, each observation represents a centerline pixel in which arteries pixels are 30048 and the remaining 31924 are veins. A set of 34 local features, listed in Table 2 have been computed for each centerline pixel in the training images. Some of these features are earlier been used by [107, 108] and [109], and offers the best performance measures. The selection of features has reduced performance on the training set, so the whole set of features is used for experiments on test data. All the processing steps including vasculature segmentation, vessel skeletonization, and measurement of

junction points for vessel and centerline segment extraction as detailed in Section 3.1, 3.2 and 3.3 respectively, are applied to all images in the training set.

To select a suitable classifier for our experiments, we divided the training set into a distinct classifier selection test and training set. A comprehensive comparison of different classifiers such as bagging classifier, k-nearest neighbor classifier, adaboostM1 classifier, and logit boost classifier has performed. A classifier that has improved the receiver operator characteristic (ROC) area [110] was picked. This experiment showed that bagging classifier offers best results as shown in Table 3, and selected for training our system.

Table 3 Classifier selection based on ROC curve area.

No.	Classifier Name	T-P Rate	F-P Rate	Precision	Recall	F-Measure	ROC Area
1	Bagging (with 300 Decision trees)	90.4	10.1	91.6	90.4	90.3	97.9
2	LogitBoost (with 300 Fast Decision Trees Learner)	90.4	10.2	91.6	90.4	90.2	97.8
3	AdaBoostM1 (Random Forest)	90.3	10.3	91.5	90.3	90.2	97.7
4	K Nearest Neighbour (K=1, Cosine Distance)	90	10.6	91.1	90	89.9	97.1

3.4.4 Applying the AV Classification to Unseen Data

In the testing phase, the previously trained classifier is used to predict arteries and veins in unseen images. We used leave-one-out cross-validation testing technique [111]. All images of the test set were normalized and preprocessed likewise training images. A set of 34 features was computed for each centerline pixel and previously trained classifier was then used to assign a soft label to each of them. These soft labels are also known as probability score. If probability score of a pixel was near to 0 meant that the pixel was expected in an artery and if close to 1 meant that pixel was probably in a vein. We supposed that all pixels in vessel segments are either artery pixels or vein pixels. Soft labels of centerline segment

pixels were used as a vote for labeling of the vessel segment. Combining these votes can be done by a verity of methods, some researchers used the medium value of soft labels. To perform final classification, we count soft labels of arteries and veins of centerline segment pixels and label to vessel segment was assigned based on more than 50% votes in a category.
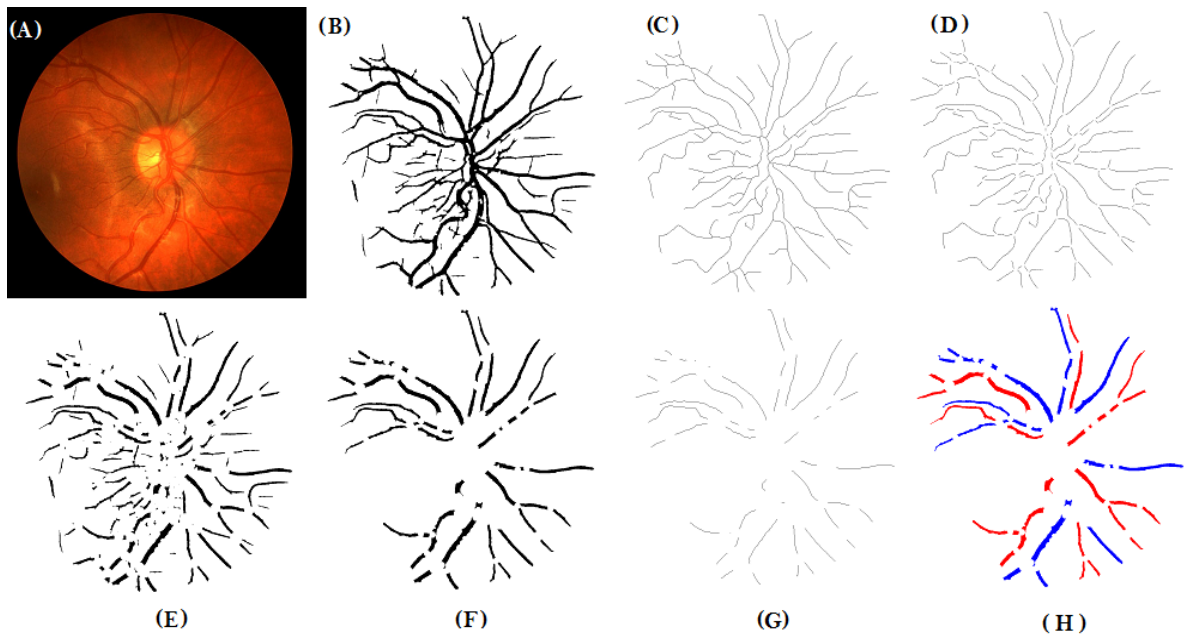
Fig. 20. Demonstration of the proposed methodology: (A) is an original image of CHASE_DB1(Image12R.jpg). (B) shows blood vessel segmented by B-COSFIRE filter. (C) is skeletonization of (B), extracted by fast marching method. (D) represents single pixel centerline segments, junction points are detected in (C) and removed in (D). Every junction point in (B) is treated like a bifurcation, and the detected bifurcation points are then dilated and removed. (E) illustrates the result of removing bifurcation points from (B). In (E), objects having less than 60-pixel area were excluded to reduce false classification, but we have to take care of major vessels the one labeled by expert, result is represented by (F). Similarly, in (D) less than 30-pixel objects are excluded, also, care has been taken of centerline pixels of major vessels, the result is shown by(G). (H) represents final classification result, red shows arteries while blue represents veins.

Chapter 4

Experiments and Results

4.1 Experiments

We have used Matlab (version 2015a) toolboxes such as: "Image Processing Toolbox", "Statistics and Machine Learning Toolbox", and "Global Optimization Toolbox" to implement the algorithm. A core i3 processor based laptop having 4GB RAM and 500GB HD has been used for experiments. After onetime training the classifier, it took approximately 2-minutes on the parallel computing-based system to extract features from inputted test image and acquire predicted results using the trained classifier.

To reduce false classification, we have excluded small vessels and their segments. We consider only major vessels to be classified. Before extracting features from an image, we preprocessed vessels segments and their centerline pixels. Vessel segments having less than 60-pixel area were excluded but It has been tried not to disturb major vessel segment while applying this condition. Similarly, in centerline pixel image, less than 30-pixels objects were excluded. These results are illustrated by Fig. 20(F) and Fig. 20(G)

4.2 Materials

A publicly available dataset has been used for experiments. The CHASE_DB1 [112] is a retinal vessel reference dataset captured in 46 schools from 14 multiethnic children during

a survey called "Child Heart and Health Study in England (CHASE)". The purpose of the survey was to highlight retinal vessel tortuosity association with cardiovascular disease in over 1000 different ethnic origin primary schools of England [17]. Hand-held Nidek NM-200-D fundus camera has been used to capture retinal images of both of the eyes of a subject. Each image of the dataset is captured at 30-degree FOV with 1280×960 resolution. Background of all images are described as non-uniformly illuminated and blood vessels are poorly contrasted as compared with the background and wider artery that have a bright strip running down the center known as the central vessel reflex.

4.3 Performance Measures

In the retinal vessel binary classification process, any pixel is classified either as artery or vein. Therefore, there is the possibility of four events: two classifications and two misclassifications which are organized in a confusion matrix, shown in Table 4

Table 4 A/V evaluation matrix.

A/V algorithm result	Artery	Vein
Artery-detected	True-Artery(TP)	False-Artery(FP)
Vein-detected	False-Vein(FN)	True-Vein(TN)

To measure how much efficient and robust a classifier is, we used some performance parameters presented in Table 5. These parameters are also used elsewhere [113].

Table 5 Performance Metrics for Artery/Vein classification using the notation of Table 4.

Measure	Formula	Description
ACC^{*}	$$\frac{TP+TN}{TP+FN+FP+FN}$$	Shows overall effectiveness of a model
Sensitivity (Se)/Recall	$$\frac{TP}{TP+FN}$$	Efficiency of a classification model to recognize positive labels
Specificity (Sp)	$$\frac{TN}{TN+FP}$$	How successfully a classification model identifies negative labels
MCC^{**}	$$\frac{TP \times TN - FP \times FN}{\sqrt{(TP+FP)(TP+FN)(TN+FP)(TN+FN)}}$$	A correlation coefficient between the experimental and predicted binary classifications.
Precision (Pre)	$$\frac{TP}{TP+FP}$$	Class agreement of the data labels with the positive labels given by the classifier
F-Score (F-m)	$$\frac{2 \times recall \times precision}{(recall + precision)}$$	Relations between data's positive labels and those given by a classifier

*ACC = Overall Accuracy, **MCC = Matthews correlation coefficient,

4.4 Quantitative Results

We have used bootstrap aggregating to predict A/V in unseen image data of CHASE_DB1. For demonstration, Image_12R of CHASE_DB1 is used to test our developed algorithm. There are two expected predictions such as 0 (artery pixel) and 1 (vein pixel). Overall accuracy was accomplished 77.194 for this specific unseen sample. Correct A/V classification result of the example Image_12R retinal vasculature is plotted by Fig. 20(H) while misclassification is omitted from plotting. Fig. 20 demonstrates results of the proposed methodology. Table 6 shows Accuracy, Precision, Recall, Specificity, F-score, and MCC values computed from processed bagging predictions using jackknife testing technique [111].

4.4.1 Comparison with Relevant Approach

The proposed decision trees based ensemble classification model is compared against cosine similarity-based k-nearest neighbors(KNN) classifier [114, 115]. Jackknife testing technique has been used to validate bagging and the KNN model. This test is also known as leave-one-out cross-validation in which each image of the dataset is used for testing and at the same time the remaining dataset is used for training the model. Table 6 gives you an idea about the predictive performance of our approach. It has comparatively higher accuracy and a low standard deviation of accuracy against KNN performance described in Table 7. The reasons are the effectiveness of the color-based features for the classification and the discriminative power of bagging and KNN. Lost analysis of the training set as plotted by Fig. 22 has been used to constructed a single nearest neighbor cosine distance based KNN model. Predicted measurements of the bagging and the KNN classifier are graphically represented by Fig. 21 and Fig. 23, respectively. This analysis exhibits that bagging offers the best accuracy and prominent variance in accuracies.

Table 6 Jackknife Test is performed for validation of Decision Trees based bagging model.

Image Name	Accuracy %	Precision %	Recall %	FMeasure %	Specificity %	MCC %
Image_01L.jpg	67.06	75.90	50.00	60.29	84.13	36.31
Image_01R.jpg	76.84	80.10	71.43	75.52	82.26	54.00
Image_02L.jpg	73.89	88.98	54.55	67.63	93.24	51.83
Image_02R.jpg	89.52	82.68	96.00	90.52	79.05	80.84
Image_03L.jpg	73.15	82.21	59.09	68.76	87.21	48.25
Image_03R.jpg	73.93	83.88	59.26	69.45	88.61	50.07
Image_04L.jpg	67.02	68.96	61.90	65.24	72.13	34.22
Image_04R.jpg	71.89	80.40	57.89	67.31	85.88	45.60
Image_05L.jpg	72.52	82.01	57.69	67.73	87.34	47.15
Image_05R.jpg	73.19	79.96	61.90	69.78	84.48	47.62
Image_06R.jpg	74.44	83.68	60.71	70.37	88.16	50.82
Image_08L.jpg	86.71	79.00	94.00	88.27	73.42	76.16

Image_08R.jpg	80.65	72.09	90.00	83.78	61.29	66.47
Image_09L.jpg	68.32	81.27	47.62	60.05	89.02	40.26
Image_10L.jpg	71.23	82.82	53.57	65.06	88.89	45.39
Image_10R.jpg	75.07	84.37	61.54	71.17	88.60	52.08
Image_11L.jpg	62.25	73.38	38.46	50.47	86.05	27.87
Image_11R.jpg	64.29	75.00	42.86	54.55	85.71	31.62
Image_12L.jpg	85.38	77.38	94.00	87.25	70.77	74.00
Image_12R.jpg	76.65	86.02	63.64	73.15	89.66	55.19
Image_13R.jpg	65.72	83.57	39.13	53.30	92.31	37.12
Image_14L.jpg	69.58	82.18	50.00	62.17	89.16	42.55
Image_14R.jpg	80.61	72.06	90.00	83.76	61.22	66.42
Average	73.91	79.91	63.27	69.81	82.98	50.51
Standard Deviation	6.92	4.88	28.28	10.82	8.90	13.89
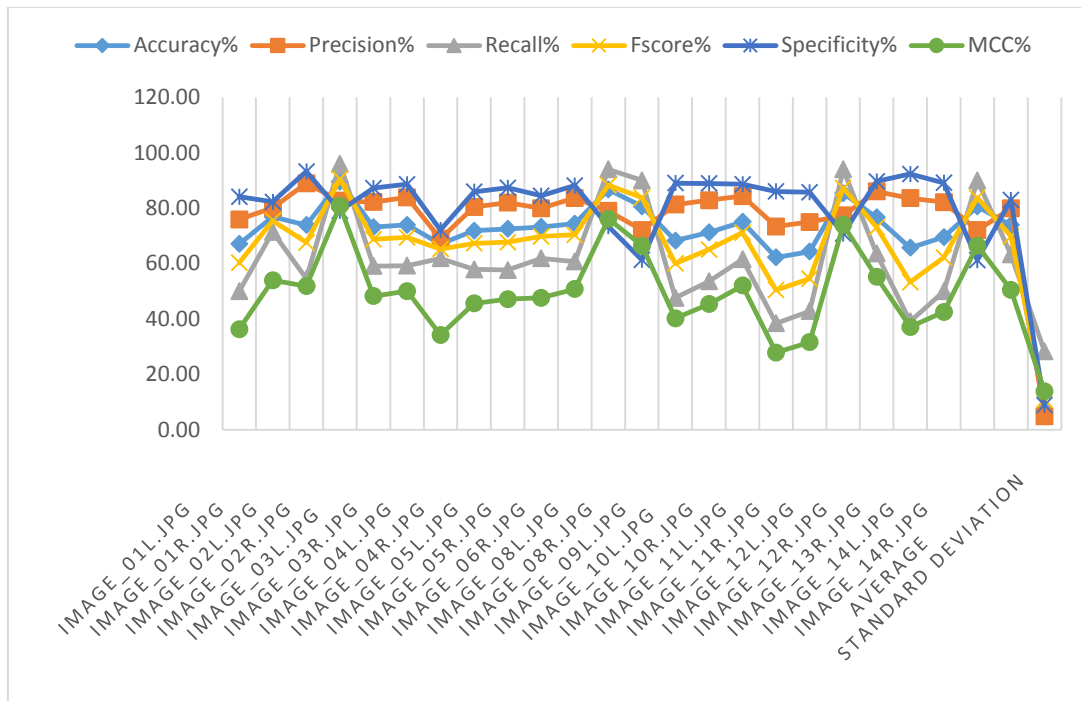
Fig. 21. Illustration of Leave-one-out cross-validation predictions using bagging.
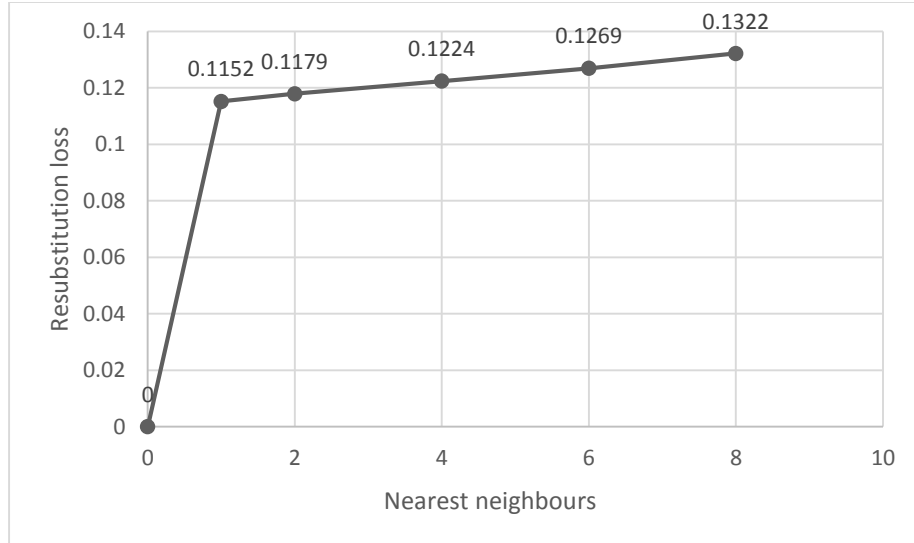
Fig. 22 KNN classification loss analysis for nearest neighbors.

Table 7 Predictive performance of cosine distance based KNN model using Jackknife Test.

Image Name	Accuracy%	Precision%	Recall%	Fscore%	Specificity%	MCC%
Image_01L.jpg	70.63	77.66	60.71	68.15	82.54	44.32
Image_01R.jpg	71.35	84.41	52.38	64.64	90.32	46.15
Image_02L.jpg	71.89	88.98	54.55	67.63	93.24	51.83
Image_02R.jpg	86.52	82.68	92.34	90.52	79.05	80.84
Image_03L.jpg	70.30	79.63	54.55	64.74	86.05	42.77
Image_03R.jpg	71.08	82.98	55.56	66.55	88.61	46.79
Image_04L.jpg	63.90	68.05	52.38	59.20	75.41	28.56
Image_04R.jpg	69.85	80.26	52.63	63.58	87.06	42.27
Image_05L.jpg	72.54	78.90	61.54	69.15	83.54	46.22
Image_05R.jpg	68.64	82.15	47.62	60.29	89.66	41.08
Image_06R.jpg	60.62	71.16	35.71	47.56	85.53	24.50
Image_08L.jpg	84.71	79.00	91.54	88.27	73.42	76.16
Image_08R.jpg	80.65	72.09	90.12	83.78	61.29	66.47
Image_09L.jpg	76.07	86.39	61.90	72.12	90.24	54.38
Image_10L.jpg	80.78	87.85	71.43	78.79	90.12	62.66
Image_10R.jpg	73.63	83.36	61.54	70.81	87.72	51.04
Image_11L.jpg	76.06	82.08	69.23	75.11	84.88	54.79
Image_11R.jpg	59.52	70.00	33.33	45.16	85.71	22.36
Image_12L.jpg	84.38	77.38	91.12	87.25	70.77	74.00
Image_12R.jpg	73.92	82.19	63.64	71.73	86.21	51.16
Image_13R.jpg	78.80	85.73	73.91	79.38	87.69	62.20
Image_14L.jpg	73.23	83.84	62.50	71.61	87.95	52.17

Image_14R.jpg	80.61	72.06	90.13	83.76	61.22	66.42
Average	73.90	79.95	64.36	70.86	82.97	51.70
Standard Deviation	7.16	5.72	17.23	11.55	8.65	15.01
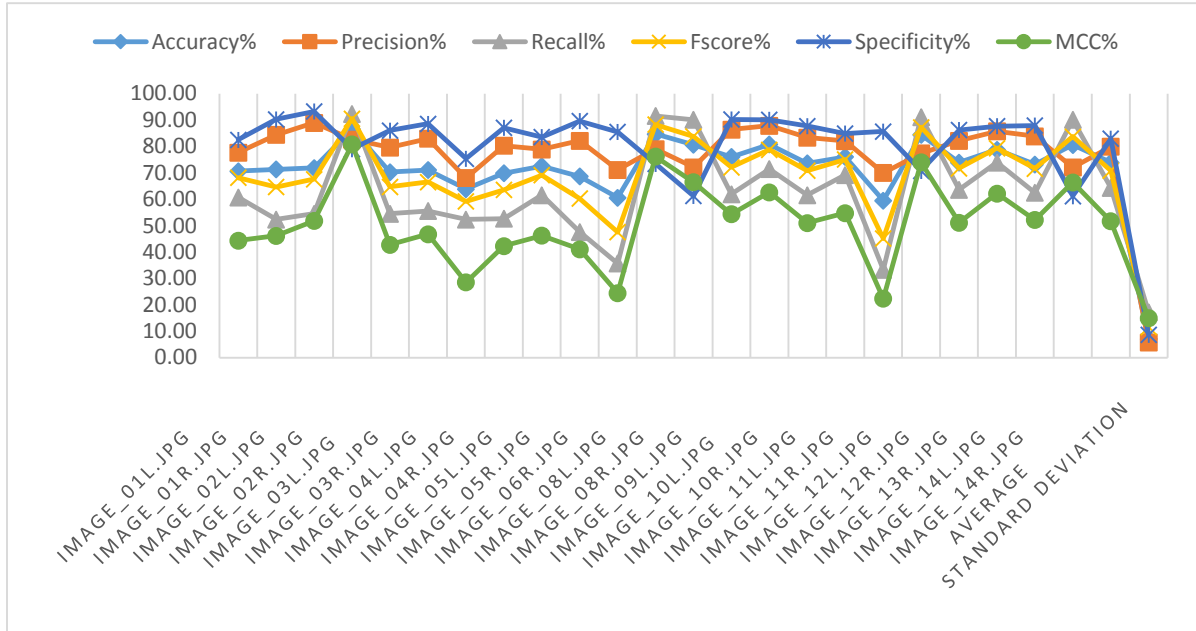
Fig. 23. Graphical representation of leave-one-out cross-validation of KNN model.

The A/V classification result with the best case and worst case accuracies from the CHASE_DB1 database are illustrated in Fig. *24*. The best case accuracy, precision, recall, f-measure, specificity and MCC are 80.65, 72.09, 90.00, 83.78, 61.29 and 66.47, respectively, and the worst case measures are 62.25, 73.38, 38.46, 50.47, 86.05, and 27.87, respectively.
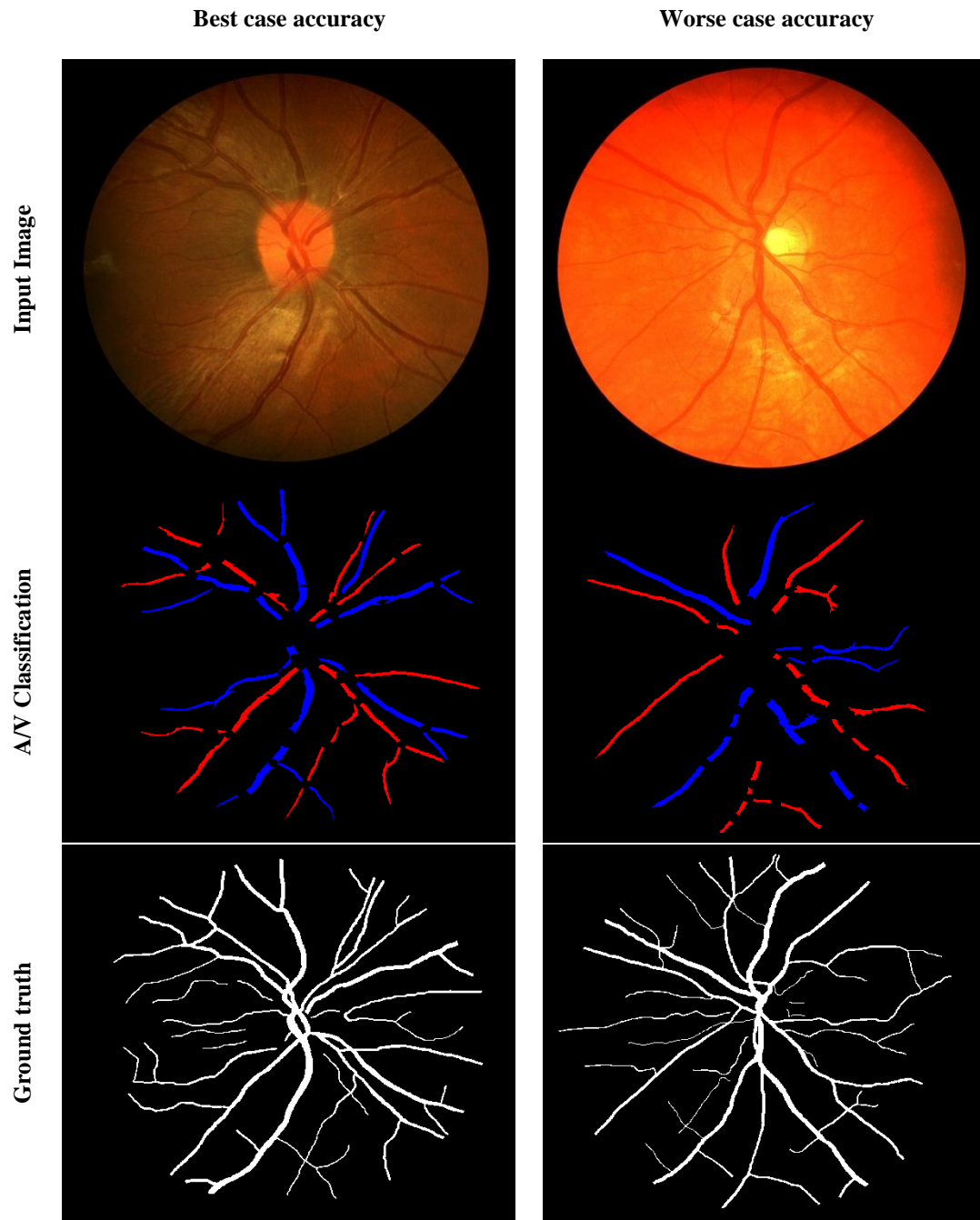
Fig. 24. Classification results of ensemble based model. Red are arteries while blue are veins.

Chapter 5

Discussion and Conclusion

The retinal blood vessels are clinically significant because it exhibits typical alterations in ocular disease and their properties can be used as biomarkers for the general state of health and systemic diseases. A/V classification is crucial for arteriolar-to-venular diameter ratio (AVR). Precisely, a low AVR, i.e., narrowing of the retinal arteries or/and spreading of the retinal veins, is significantly connected with a high risk of myocardial infarction and stroke. Furthermore, a recent research article has revealed that a reduced AVR is associated with, dyslipidemia, obesity, hyperglycemia, and smoking [116]. Computation of AVR from classified arteries and veins can be used for automatic analysis of diabetic retinopathy. Vasculature abnormalities such as dilating of veins and caliber changes occur in diabetic retinopathy. Similarly, atherosclerosis and hypertension cause retinal blood vessel changes such as the thinning of arterioles and the dilation of venules.

We have used Matlab's image processing and machine learning toolboxes to implement our algorithm. To classify retinal vessels into arteries and veins, we pass through some algorithmic steps: first of all, retinal vasculature was segmented using an advanced algorithm called B-COSFIRE, retinal skeletonization of the segmented vasculature was then computed using fast marching method to get vessels centerline pixels. Segmented vasculature and centerline pixels are divided at junction points to extract their segments.

Finally, centerline pixels are classified using ensemble based classifier and more than 50% labeled pixels based criteria is used to label a particular vessels segment. A classified vasculature tree was built iteratively going through labeled vessel segments.

In conclusion, many systemic diseases are directly associated with morphological structure changes of the arteries and veins. Automatic detection of these structural changes of retinal blood vessels would lead to an automatic analysis of a particular disease. To detect a specific systemic disease from retinal blood vessels, the first step is to accurately separate arteries and veins. In this study, we presented a framework to automatically classify arteries and veins from retinal digital fundus images. Our work could be used as a baseline for automatic identification and analysis of a particular systemic disease. We have employed machine learning and image processing techniques in Matlab for retinal blood vessel analysis and classification into arteries and veins. For vessels classification, an ensemble based model is used which offered the best accuracy as compared to a relative approach. According to the best of our knowledge, this is the first research article who used CHASE_DB1 dataset and ensemble based classifier for A/V classification.

5.1 Future Directions

This work can be used for automatic analysis of a systemic disease. Our classification results can be compared with other classification performances to measure the effectiveness of different classifiers. False classification needs to be reduced in this study. There should be some more accurate and intelligent strategy which can reduce deletion of small objects of major vessels while removing the small objects.

References

[1] N. Patton, T. M. Aslam, T. MacGillivray, I. J. Deary, B. Dhillon, R. H. Eikelboom*, et al.*, "Retinal image analysis: Concepts, applications and potential," *Progress in Retinal and Eye Research,* vol. 25, pp. 99-127, 1// 2006.

[2] C. Y.-l. Cheung, M. K. Ikram, C. Sabanayagam, and T. Y. Wong, "Retinal Microvasculature as a Model to Study the Manifestations of Hypertension," *Hypertension,* vol. 60, pp. 1094-1103, November 1, 2012 2012.

[3] M. K. Ikram, C. Y. Cheung, M. Lorenzi, R. Klein, T. L. Z. Jones, T. Y. Wong*, et al.*, "Retinal Vascular Caliber as a Biomarker for Diabetes Microvascular Complications," *Diabetes Care,* vol. 36, pp. 750-759, March 1, 2013 2013.

[4] A. S. NEUBAUER, M. LÜDTKE, C. HARITOGLOU, S. PRIGLINGER, and A. KAMPIK, "Retinal Vessel Analysis Reproducibility in Assessing Cardiovascular Disease," *Optometry & Vision Science,* vol. 85, pp. E247-E254, 2008.

[5] B. Dashtbozorg, A. M. Mendon, x00E, and A. Campilho, "An automatic method for the estimation of Arteriolar-to-Venular Ratio in retinal images," in *Computer-Based Medical Systems (CBMS), 2013 IEEE 26th International Symposium on*, 2013, pp. 512-513.

[6] J. J. Wang, G. Liew, R. Klein, E. Rochtchina, M. D. Knudtson, B. E. K. Klein*, et al.*, "Retinal vessel diameter and cardiovascular mortality: pooled data analysis from two older populations," *European Heart Journal,* vol. 28, pp. 1984-1992, 2007-08-01 00:00:00 2007.

[7] M. K. Ikram, F. J. de Jong, J. R. Vingerling, J. C. M. Witteman, A. Hofman, M. M. B. Breteler*, et al.*, "Are Retinal Arteriolar or Venular Diameters Associated with Markers for Cardiovascular Disorders? The Rotterdam Study," *Investigative Ophthalmology & Visual Science,* vol. 45, pp. 2129-2134, 2004.

[8] C. Kondermann, D. Kondermann, and M. Yan, "Blood vessel classification into arteries and veins in retinal images," in *Proc. SPIE Progr. Biomed. Opt. Imag*, 2007, pp. 651247-651247-9.

[9] R. Klein, B. K. Klein, M. D. Knudtson, T. Y. Wong, and M. Y. Tsai, "Are inflammatory factors related to retinal vessel caliber?: The beaver dam eye study," *Archives of Ophthalmology,* vol. 124, pp. 87-94, 2006.

[10] J. S. Wolffsohn, G. A. Napper, S.-M. Ho, A. Jaworski, and T. L. Pollard, "Improving the description of the retinal vasculature and patient history taking for monitoring systemic hypertension," *Ophthalmic and Physiological Optics,* vol. 21, pp. 441-449, 2001.

[11] N. CHAPMAN, G. DELL'OMO, M. S. SARTINI, N. WITT, A. HUGHES, S. THOM*, et al.*, "Peripheral vascular disease is associated with abnormal arteriolar diameter relationships at bifurcations in the human retina," *Clinical Science,* vol. 103, pp. 111-116, 2002-08-01 00:00:00 2002.

[12] A. V. S. e. al, "Vascular network changes in the retina with age and hypertension," *J. Hypertens,* vol. 13, pp. 1724–1728 1995.

[13] R. S. Snell and M. A. Lemp, *Clinical Anatomy of the Eye*: Wiley, 1997.

[14] *The Retina Reference*. Available: http://www.retinareference.com/

[15] G. Azzopardi, N. Strisciuglio, M. Vento, and N. Petkov, "Trainable COSFIRE filters for vessel delineation with application to retinal images," *Medical Image Analysis,* vol. 19, pp. 46-57, 1// 2015.

[16] R. Van Uitert and I. Bitter, "Subvoxel precise skeletons of volumetric data based on fast marching methods," *Medical Physics,* vol. 34, pp. 627-638, 2007.

[17] C. G. Owen, A. R. Rudnicka, R. Mullen, S. A. Barman, D. Monekosso, P. H. Whincup*, et al.*, "Measuring Retinal Vessel Tortuosity in 10-Year-Old Children: Validation of the

Computer-Assisted Image Analysis of the Retina (CAIAR) Program," *Investigative Ophthalmology & Visual Science,* vol. 50, pp. 2004-2010, 2009.

[18] B. Bouma, *Handbook of Optical Coherence Tomography*: Taylor & Francis, 2001.

[19] J. S. Schuman, "Spectral Domain Optical Coherence Tomography for Glaucoma (An AOS Thesis)," *Transactions of the American Ophthalmological Society,* vol. 106, pp. 426-458, 2008.

[20] R. K. Wang and V. V. Tuchin, *Advanced Biophotonics: Tissue Optical Sectioning*: Taylor & Francis, 2013.

[21] J. Xu, H. Ishikawa, G. Wollstein, and J. S. Schuman, "3D Optical Coherence Tomography Super Pixel with Machine Classifier Analysis for Glaucoma Detection," *Conference Proceedings,* vol. 2011, pp. 3395-3398, 2011.

[22] R. Liang, *Biomedical Optical Imaging Technologies: Design and Applications*: Springer Berlin Heidelberg, 2012.

[23] M. R. Hee, J. A. Izatt, E. A. Swanson, D. Huang, J. S. Schuman, C. P. Lin*, et al.*, "Optical coherence tomography of the human retina," *Archives of Ophthalmology,* vol. 113, pp. 325-332, 1995.

[24] D. Huang, E. A. Swanson, C. P. Lin, J. S. Schuman, W. G. Stinson, W. Chang*, et al.*, "Optical coherence tomography," *Science,* vol. 254, pp. 1178-1181, 1991.

[25] H. C. Fercher AF, Drexler W, Kamp G, Sattmann H., "In vivo optical coherence tomography," vol. Am J Ophthalmol. 1993 Jul 15;116(1):113-4.

[26] B. M. Fujimoto JG1, Tearney GJ, Boppart SA, Bouma B, Hee MR, Southern JF, Swanson EA., "Optical biopsy and imaging using optical coherence tomography.," *Nat Med. 1995 Sep;1(9):970-2.*

[27] M. Wojtkowski, V. Srinivasan, J. G. Fujimoto, T. Ko, J. S. Schuman, A. Kowalczyk*, et al.*, "Three-dimensional Retinal Imaging with High-Speed Ultrahigh-Resolution Optical Coherence Tomography," *Ophthalmology,* vol. 112, pp. 1734-1746, 10// 2005.

[28] J. W. Zahid Yaqoob, and Changhuei Yang "Spectral domain optical coherence tomography: a better OCT imaging strategy," vol. BioTechniques, Vol. 39, No. 6, December 2005, pp. S6–S13.

[29] W. Drexler and J. G. Fujimoto, "State-of-the-art retinal optical coherence tomography," *Progress in Retinal and Eye Research,* vol. 27, pp. 45-88, 1// 2008.

[30] M. Wojtkowski, "High-speed optical coherence tomography: basics and applications," *Applied Optics,* vol. 49, pp. D30-D61, 2010/06/01 2010.

[31] M. Wojtkowski, T. Bajraszewski, P. Targowski, and A. Kowalczyk, "Real-time in vivo imaging by high-speed spectral optical coherence tomography," *Optics Letters,* vol. 28, pp. 1745-1747, 2003/10/01 2003.

[32] S. Yun, G. Tearney, B. Bouma, B. Park, and J. de Boer, "High-speed spectral-domain optical coherence tomography at 1.3 ?m wavelength," *Optics Express,* vol. 11, pp. 3598-3604, 2003/12/29 2003.

[33] N. Nassif, B. Cense, B. Hyle Park, S. H. Yun, T. C. Chen, B. E. Bouma*, et al.*, "In vivo human retinal imaging by ultrahigh-speed spectral domain optical coherence tomography," *Optics Letters,* vol. 29, pp. 480-482, 2004/03/01 2004.

[34] T. Bajraszewski, M. Wojtkowski, M. Szkulmowski, A. Szkulmowska, R. Huber, and A. Kowalczyk, "Improved spectral optical coherence tomography using optical frequency comb," *Optics Express,* vol. 16, pp. 4163-4176, 2008/03/17 2008.

[35] B. Potsaid, I. Gorczynska, V. J. Srinivasan, Y. Chen, J. Jiang, A. Cable*, et al.*, "Ultrahigh speed Spectral / Fourierdomain OCT ophthalmic imaging at70,000 to 312,500 axial scans per second," *Optics Express,* vol. 16, pp. 15149-15169, 2008/09/15 2008.

[36] I. Grulkowski, M. Gora, M. Szkulmowski, I. Gorczynska, D. Szlag, S. Marcos*, et al.*, "Anterior segment imaging with Spectral OCT system using a high-speed CMOS camera," *Optics Express,* vol. 17, pp. 4842-4858, 2009/03/16 2009.

[37]   A. Szkulmowska, M. Szkulmowski, D. Szlag, A. Kowalczyk, and M. Wojtkowski, "Three-dimensional quantitative imaging?of retinal and choroidal blood flow velocity using joint Spectral and Time domain Optical Coherence Tomography," *Optics Express,* vol. 17, pp. 10584-10598, 2009/06/22 2009.

[38]   M. Choma, M. Sarunic, C. Yang, and J. Izatt, "Sensitivity advantage of swept source and Fourier domain optical coherence tomography," *Optics Express,* vol. 11, pp. 2183-2189, 2003/09/08 2003.

[39]   S. H. Yun, C. Boudoux, G. J. Tearney, and B. E. Bouma, "High-speed wavelength-swept semiconductor laser with a polygon-scanner-based wavelength filter," *Optics Letters,* vol. 28, pp. 1981-1983, 2003/10/15 2003.

[40]   R. Huber, M. Wojtkowski, J. G. Fujimoto, J. Y. Jiang, and A. E. Cable, "Three-dimensional and C-mode OCT imaging with a compact, frequency swept laser source at 1300 nm," *Optics Express,* vol. 13, pp. 10523-10538, 2005/12/26 2005.

[41]   S.-W. Huang, A. D. Aguirre, R. A. Huber, D. C. Adler, and J. G. Fujimoto, "Swept source optical coherence microscopy using a Fourier domain mode-locked laser," *Optics Express,* vol. 15, pp. 6210-6217, 2007/05/14 2007.

[42]   B. Golubovic, B. E. Bouma, G. J. Tearney, and J. G. Fujimoto, "Optical frequency-domain reflectometry using rapid wavelength tuning of a Cr4+:forsterite laser," *Optics Letters,* vol. 22, pp. 1704-1706, 1997/11/15 1997.

[43]   S. Yun, G. Tearney, J. de Boer, N. Iftimia, and B. Bouma, "High-speed optical frequency-domain imaging," *Optics Express,* vol. 11, pp. 2953-2963, 2003/11/03 2003.

[44]   W. Y. Oh, S. H. Yun, G. J. Tearney, and B. E. Bouma, "115 kHz tuning repetition rate ultrahigh-speed wavelength-swept semiconductor laser," *Optics Letters,* vol. 30, pp. 3159-3161, 2005/12/01 2005.

[45]   W. Y. Oh, S. H. Yun, B. J. Vakoc, G. J. Tearney, and B. E. Bouma, "Ultrahigh-speed optical frequency domain imaging and application to laser ablation monitoring," *Applied Physics Letters,* vol. 88, pp. 103902-103902-3, 2006.

[46]   I. V. Larina, K. Furushima, M. E. Dickinson, R. R. Behringer, and K. V. Larin, "Live imaging of rat embryos with Doppler swept-source optical coherence tomography," *Journal of Biomedical Optics,* vol. 14, pp. 050506-050506-3, 2009.

[47]   A. Mariampillai, B. A. Standish, N. R. Munce, C. Randall, G. Liu, J. Y. Jiang*, et al.*, "Doppler optical cardiogram gated 2D color flow imaging at 1000 fps and 4D in vivo visualization of embryonic heart at 45 fps on a swept source OCT system," *Optics Express,* vol. 15, pp. 1627-1638, 2007/02/19 2007.

[48]   R. Huber, M. Wojtkowski, K. Taira, J. Fujimoto, and K. Hsu, "Amplified, frequency swept lasers for frequency domain reflectometry and OCT imaging: design and scaling principles," *Optics Express,* vol. 13, pp. 3513-3528, 2005/05/02 2005.

[49]   M. A. Choma, K. Hsu, and J. A. Izatt, "Swept source optical coherence tomography using an all-fiber 1300-nm ring laser source," *Journal of Biomedical Optics,* vol. 10, pp. 044009-044009-6, 2005.

[50]   R. Huber, M. Wojtkowski, and J. G. Fujimoto, "Fourier Domain Mode Locking (FDML): A new laser operating regime and applications for optical coherence tomography," *Optics Express,* vol. 14, pp. 3225-3237, 2006/04/17 2006.

[51]   R. Huber, D. C. Adler, V. J. Srinivasan, and J. G. Fujimoto, "Fourier domain mode locking at 1050 nm for ultra-high-speed optical coherence tomography of the human retina at 236,000 axial scans per second," *Optics Letters,* vol. 32, pp. 2049-2051, 2007/07/15 2007.

[52]   B. R. Biedermann, W. Wieser, C. M. Eigenwillig, T. Klein, and R. Huber, "Dispersion, coherence and noise of Fourier domain mode locked lasers," *Optics Express,* vol. 17, pp. 9947-9961, 2009/06/08 2009.

[53]   (March-2015). *3D OCT-1 Maestro, Optical Coherence Tomography*. Available: http://www.topcon-medical.eu/eu/products/253-3d-oct-1-maestro-optical-coherence-tomography.html

[54]   (March 2015). *DRI OCT-1, Atlantis swept source OCT*. Available: http://www.topcon-medical.eu/eu/products/177-dri-oct-1-atlantis-swept-source-oct.html

[55]   *Carl Zeiss Meditec*. Available: http://www.zeiss.com/meditec/en_de/home.html

[56]   *Topcon* Available: http://www.topcon-medical.eu/eu/

[57]   *Heidelberg Engineering*. Available: https://www.heidelbergengineering.com/us/

[58]   *NIDEK CO*. Available: http://www.nidek-intl.com/

[59]   *Optovue Inc*. Available: http://optovue.com/

[60]   *Which OCT should I buy*. Available: www.oftalmolog.com/Sider/artikDec10/Which.pdf

[61]   C. Jun, L. Jiang, X. Yanwu, Y. Fengshou, D. W. K. Wong, T. Ngan-Meng*, et al.*, "Superpixel Classification Based Optic Disc and Optic Cup Segmentation for Glaucoma Screening," *Medical Imaging, IEEE Transactions on,* vol. 32, pp. 1019-1032, 2013.

[62]   J. L. Keltner, C. A. Johnson, J. M. Quigg, C. KE., K. MA., and Gordon MO., "COnfirmation of visual field abnormalities in the ocular hypertension treatment study," *Archives of Ophthalmology,* vol. 118, pp. 1187-1194, 2000.

[63]   I. I. Bussel, G. Wollstein, and J. S. Schuman, "OCT for glaucoma diagnosis, screening and detection of glaucoma progression," *The British Journal of Ophthalmology,* vol. 98, pp. ii15-ii19, 12/19 09/13/received 11/07/revised 11/13/accepted 2014.

[64]   J. Xu, H. Ishikawa, G. Wollstein, R. A. Bilonick, L. S. Folio, Z. Nadler*, et al.*, "Three-Dimensional Spectral-Domain Optical Coherence Tomography Data Analysis for Glaucoma Detection," *PLoS ONE,* vol. 8, p. e55476, 02/11 09/19/received 12/23/accepted 2013.

[65]   M. D. Abramoff, M. K. Garvin, and M. Sonka, "Retinal Imaging and Image Analysis," *Biomedical Engineering, IEEE Reviews in,* vol. 3, pp. 169-208, 2010.

[66]   Z. Hu, M. D. Abràmoff, Y. H. Kwon, K. Lee, and M. K. Garvin, "Automated Segmentation of Neural Canal Opening and Optic Cup in 3D Spectral Optical Coherence Tomography Volumes of the Optic Nerve Head," *Investigative Ophthalmology & Visual Science,* vol. 51, pp. 5708-5717, 10/28/received 04/14/revised 05/18/revised 05/25/accepted 2010.

[67]   L. Kyungmoo, M. Niemeijer, M. K. Garvin, Y. H. Kwon, M. Sonka, and M. D. Abramoff, "Segmentation of the Optic Disc in 3-D OCT Scans of the Optic Nerve Head," *Medical Imaging, IEEE Transactions on,* vol. 29, pp. 159-168, 2010.

[68]   K. Lee, M. Niemeijer, M. K. Garvin, Y. H. Kwon, M. Sonka, and M. D. Abràmoff, "3-D segmentation of the rim and cup in spectral-domain optical coherence tomography volumes of the optic nerve head," 2009, pp. 72622D-72622D-9.

[69]   M. D. Abràmoff, K. Lee, M. Niemeijer, W. L. M. Alward, E. C. Greenlee, M. K. Garvin*, et al.*, "Automated Segmentation of the Cup and Rim from Spectral Domain OCT of the Optic Nerve Head," *Investigative Ophthalmology & Visual Science,* vol. 50, pp. 5778-5784, December 1, 2009 2009.

[70]   Z. Hu, M. Niemeijer, K. Lee, M. D. Abràmoff, M. Sonka, and M. K. Garvin, "Automated segmentation of the optic disc margin in 3-D optical coherence tomography images using a graph-theoretic approach," 2009, pp. 72620U-72620U-11.

[71]   H. Z. Kwon Y, Abramoff M, Lee K, Garvin M. , "Automated segmentation of neural canal opening and optic cup in SD-OCT images," *Annual Am Glaucoma Soc Meeting.,* 2010 March.

[72]   Z. H. a. M. N. a. K. L. a. M. D. A. a. M. S. a. M. K. Garvin, "Automated Segmentation of the Optic Canal in 3D Spectral-Domain OCT of the Optic Nerve Head (ONH) Using Retinal Vessel Suppression," *Association for Research in Vision and Ophthalmology (ARVO),* 2010.

[73]   B. J. Curtin, "The posterior staphyloma of pathologic myopia," *Trans Am Ophthalmol Soc,* vol. 75, pp. 67-86, 1977.

[74]   Y. Imamura, T. Iida, I. Maruko, S. A. Zweifel, and R. F. Spaide, "Enhanced depth imaging optical coherence tomography of the sclera in dome-shaped macula," *Am J Ophthalmol,* vol. 151, pp. 297-302, Feb 2011.

[75]   I. Maruko, T. Iida, Y. Sugano, H. Oyamada, and T. Sekiryu, "Morphologic choroidal and scleral changes at the macula in tilted disc syndrome with staphyloma using optical coherence tomography," *Invest Ophthalmol Vis Sci,* vol. 52, pp. 8763-8, 2011.

[76]   K. Ohno-Matsui, M. Akiba, T. Modegi, M. Tomita, T. Ishibashi, T. Tokoro*, et al.*, "Association between shape of sclera and myopic retinochoroidal lesions in patients with pathologic myopia," *Invest Ophthalmol Vis Sci,* vol. 53, pp. 6046-61, Sep 2012.

[77]   L. S. Lim, G. Cheung, and S. Y. Lee, "Comparison of spectral domain and swept-source optical coherence tomography in pathological myopia," *Eye (Lond),* vol. 28, pp. 488-91, Apr 2014.

[78]   Q. D. Nguyen, D. M. Brown, D. M. Marcus, D. S. Boyer, S. Patel, L. Feiner*, et al.*, "Ranibizumab for Diabetic Macular Edema: Results from 2 Phase III Randomized Trials: RISE and RIDE," *Ophthalmology,* vol. 119, pp. 789-801, 4// 2012.

[79]   M. M. K. Muqit and P. E. Stanga, "Fourier-domain optical coherence tomography evaluation of retinal and optic nerve head neovascularisation in proliferative diabetic retinopathy," *British Journal of Ophthalmology,* vol. 98, pp. 65-72, January 1, 2014 2014.

[80]   H. Cho, A. A. Alwassia, C. V. Regiatieri, J. Y. Zhang, C. Baumal, N. Waheed*, et al.*, "RETINAL NEOVASCULARIZATION SECONDARY TO PROLIFERATIVE DIABETIC RETINOPATHY CHARACTERIZED BY SPECTRAL DOMAIN OPTICAL COHERENCE TOMOGRAPHY," *RETINA,* vol. 33, pp. 542-547, 2013.

[81]   L. Yu and Z. Chen, "Doppler variance imaging for three-dimensional retina and choroid angiography," *Journal of Biomedical Optics,* vol. 15, p. 016029, January-February02/16 09/22/received 11/25/revised 12/28/accepted 2010.

[82]   T. Iwasaki, M. Miura, C. Matsushima, M. Yamanari, S. Makita, and Y. Yasuno, "Three-dimensional optical coherence tomography of proliferative diabetic retinopathy," *British Journal of Ophthalmology,* vol. 92, p. 713, May 1, 2008 2008.

[83]   *OCT for Detecting diabetic retinoapathy* Available: http://optometrist.com.au/detecting-diabetic-retinopathy/#sthash.85X0ifbs.dpuf

[84]   *Alliance for Eye and Vision Research (AEVR).* Available: http://www.eyeresearch.org/naevr_action/oct_briefing.html

[85]   (02-July-15). *Cystoid Macular Edema (CME).* Available: http://www.kellogg.umich.edu/patientcare/conditions/cystoid.macular.edema.html

[86]   G. R. Wilkins, O. M. Houghton, and A. L. Oldenburg, "Automated Segmentation of Intraretinal Cystoid Fluid in Optical Coherence Tomography," *Biomedical Engineering, IEEE Transactions on,* vol. 59, pp. 1109-1114, 2012.

[87]   M. Miura, Y.-J. Hong, Y. Yasuno, D. Muramatsu, T. Iwasaki, and H. Goto, "Three-dimensional Vascular Imaging of Proliferative Diabetic Retinopathy by Doppler Optical Coherence Tomography," *American Journal of Ophthalmology,* vol. 159, pp. 528-538.e3, 3// 2015.

[88]   "Ophtalmology," *International Journal of Computer Assisted Radiology and Surgery,* vol. 5, pp. 28-34, 2010/06/01 2010.

[89]   G. Azzopardi and N. Petkov, "A CORF computational model of a simple cell that relies on LGN input outperforms the Gabor function model," *Biological Cybernetics,* vol. 106, pp. 177-189, 2012.

[90]   G. Azzopardi and N. Azzopardi, "Trainable COSFIRE Filters for Keypoint Detection and Pattern Recognition," *IEEE Transactions on Pattern Analysis and Machine Intelligence,* vol. 35, pp. 490-503, 2013.

[91]   H. Bium, "A TRANSFORMATION FOR EXTRACTING NEW DESCRIPTORS OF SHAPE," in *Proceedings of Models for the Perception of Speech and Visual Form*, 1967, pp. 362-380.

[92]   R. Van Uitert, I. Bitter, and J. A. Butman, "Semi-automatic spinal cord segmentation and quantification," *International Congress Series,* vol. 1281, pp. 224-229, 5// 2005.

[93]   M. Usman, M. M. Fraz, and S. A. Barman, "Computer Vision Techniques Applied for Diagnostic Analysis of Retinal OCT Images: A Review," *Archives of Computational Methods in Engineering,* pp. 1-17, 2016.

[94]   G. Troglio, A. Nappo, J. A. Benediktsson, G. Moser, S. B. Serpico, and E. Stefansson, "Automatic Change Detection of Retinal Images," in *World Congress on Medical Physics and Biomedical Engineering, September 7 - 12, 2009, Munich, Germany: Vol. 25/11 Biomedical Engineering for Audiology, Ophthalmology, Emergency & Dental Medicine*, O. Dössel and W. C. Schlegel, Eds., ed Berlin, Heidelberg: Springer Berlin Heidelberg, 2009, pp. 281-284.

[95]   J. A. Sethian, *Level Set Methods and Fast Marching Methods: Evolving Interfaces in Computational Geometry, Fluid Mechanics, Computer Vision, and Materials Science*: Cambridge University Press, 1999.

[96]   M. S. Hassouna and A. A. Farag, "MultiStencils Fast Marching Methods: A Highly Accurate Solution to the Eikonal Equation on Cartesian Domains," *IEEE Transactions on Pattern Analysis and Machine Intelligence,* vol. 29, pp. 1563-1574, 2007.

[97]   Van Uitert R. and I. Bitter, " "Subvoxel Accurate Euclidean Distance Transforms for n-dimensional Data"," *unpublished,* 2006.

[98]   M. Zamir, "Optimality principles in arterial branching," *Journal of Theoretical Biology,* vol. 62, pp. 227-251, 1976/10/07 1976.

[99]   M. J. Zamir M, "Arterial branching in man and monkey," *journal of general psychology,* vol. 79, pp. 353-360, 1982.

[100] B. Al-Diri and A. Hunter, "Automated Measurements of Retinal Bifurcations," in *World Congress on Medical Physics and Biomedical Engineering, September 7 - 12, 2009, Munich, Germany: Vol. 25/11 Biomedical Engineering for Audiology, Ophthalmology, Emergency & Dental Medicine*, O. Dössel and W. C. Schlegel, Eds., ed Berlin, Heidelberg: Springer Berlin Heidelberg, 2009, pp. 205-208.

[101] M. Zamir, "Nonsymmetrical bifurcations in arterial branching," *The Journal of General Physiology,* vol. 72, pp. 837-845, 1978.

[102] M. M. Fraz, A. R. Rudnicka, C. G. Owen, D. P. Strachan, and S. A. Barman, "Automated arteriole and venule recognition in retinal images using Ensemble classification," in *Computer Vision Theory and Applications (VISAPP), 2014 International Conference on*, 2014, pp. 194-202.

[103] I. B. M. Usman and Dauda, "Standardization and Its Effects on K-Means Clustering Algorithm," *Research Journal of Applied Sciences, Engineering and Technology,* vol. 6, pp. 3299-3303, 2013.

[104] R. Polikar, "Ensemble based systems in decision making," *IEEE Circuits and Systems Magazine,* vol. 6, pp. 21-45, 2006.

[105] L. Breiman, "Bagging Predictors," *Machine Learning,* vol. 24, pp. 123-140.

[106] M. Foracchia, E. Grisan, and A. Ruggeri, "Luminosity and contrast normalization in retinal images," *Medical Image Analysis,* vol. 9, pp. 179-190, 6// 2005.

[107] M. Niemeijer, X. Xu, A. V. Dumitrescu, P. Gupta, B. v. Ginneken, J. C. Folk*, et al.*, "Automated Measurement of the Arteriolar-to-Venular Width Ratio in Digital Color Fundus Photographs," *IEEE Transactions on Medical Imaging,* vol. 30, pp. 1941-1950, 2011.

[108] M. Niemeijer, B. van Ginneken, and M. D. Abràmoff, "Automatic determination of the artery vein ratio in retinal images," 2010, pp. 76240I-76240I-10.

[109]   B. Dashtbozorg, A. M. Mendon, x00E, and A. Campilho, "An Automatic Graph-Based Approach for Artery/Vein Classification in Retinal Images," *IEEE Transactions on Image Processing,* vol. 23, pp. 1073-1083, 2014.

[110]   C. E. METZ, "ROC Methodology in Radiologic Imaging," *Investigative Radiology,* vol. 21, pp. 720-733, 1986.

[111]   B. Efron and C. Stein, "The jackknife estimate of variance," *The Annals of Statistics,* pp. 586-596, 1981.

[112]   C. G. Owen, A. R. Rudnicka, C. M. Nightingale, R. Mullen, S. A. Barman, N. Sattar*, et al.*, "Retinal Arteriolar Tortuosity and Cardiovascular Risk Factors in a Multi-Ethnic Population Study of 10-Year-Old Children; the Child Heart and Health Study in England (CHASE)," *Arteriosclerosis, Thrombosis, and Vascular Biology,* vol. 31, pp. 1933-1938, August 1, 2011 2011.

[113]   M. Sokolova and G. Lapalme, "A systematic analysis of performance measures for classification tasks," *Information Processing & Management,* vol. 45, pp. 427-437, 7// 2009.

[114]   N. S. Altman, "An Introduction to Kernel and Nearest-Neighbor Nonparametric Regression," *The American Statistician,* vol. 46, pp. 175-185, 1992/08/01 1992.

[115]   A. Singhal, "Modern information retrieval: A brief overview," *IEEE Data Eng. Bull.,* vol. 24, pp. 35-43, 2001.

[116]   Q. Hu, M. D. Abràmoff, and M. K. Garvin, "Automated construction of arterial and venous trees in retinal images," *Journal of Medical Imaging,* vol. 2, pp. 044001-044001, 2015.